A Dexterous and Compliant (DexCo) Hand Based on Soft Hydraulic Actuation for Human-Inspired Fine In-Hand Manipulation

Jianshu Zhou, *Member, IEEE*, Junda Huang, Qi Dou, *Member, IEEE*, Pieter Abbeel, *Fellow, IEEE*, and Yunhui Liu, *Fellow, IEEE*

***Abstract*—Human beings possess a remarkable skill for fine in-hand manipulation, utilizing both intrafinger interactions (in-finger) and finger–environment interactions across a wide range of daily tasks. These tasks range from skilled activities like screwing light bulbs, picking and sorting pills, and in-hand rotation, to more complex tasks such as opening plastic bags, cluttered bin picking, and counting cards. Despite its prevalence in human activities, replicating these fine motor skills in robotics remains a substantial challenge. This study tackles the challenge of fine in-hand manipulation by introducing the dexterous and compliant (DexCo) hand system. The DexCo hand mimics human dexterity, replicating the intricate interaction between the thumb, index, and middle fingers, with a contractable palm. The key to maneuverable fine in-hand manipulation lies in its innovative soft hydraulic actuation, which strikes a balance between control complexity, dexterity, compliance, and motion accuracy within a compact structure, enhancing the overall performance of the system. The model of soft hydraulic actuation, based on hydrostatic force analysis, reveals the compliance of hand joints, which is also further extended to a dedicated robot operating system (ROS) package for DexCo hand simulation, considering both motion and stiffness aspects. Dedicated velocity and position teleoperation controllers are designed for implementing real physical manipulation tasks. The benchmark results show that the fingertip achieves a maximum repeatable finger strength of 34.4 N, a grasp cycle time of less than 2.04 s, and a maximum repeatability accuracy of 0.03 mm. Experimental results demonstrate the DexCo hand successfully performs complex fine in-hand manipulation tasks, providing a promising solution for advancing robotic manipulation capabilities toward the human level.**

Received 16 June 2024; revised 3 October 2024; accepted 10 November 2024. Date of publication 28 November 2024; date of current version 20 December 2024. This work was supported in part by the Shenzhen Portion of Shenzhen–Hong Kong Science and Technology Innovation Cooperation Zone under Grant HZQB-KCZYB-20200089, in part by the InnoHK Clusters of the Hong Kong SAR Government via the Hong Kong Centre for Logistics Robotics, and in part by the Research Grants Council of Hong Kong under Grant GRF 14207423. This article was recommended for publication by Associate Editor Van Ho and Editor Sven Behnke upon evaluation of the reviewers' comments. *(Corresponding authors: Qi Dou; Yunhui Liu.)*

Jianshu Zhou, Junda Huang, and Yunhui Liu are with the Department of Mechanical and Automation Engineering, The Chinese University of Hong Kong, Hong Kong (e-mail: jianshuzhou@cuhk.edu.hk; jdhuang99@link.cuhk.edu.hk; yhliu@cuhk.edu.hk).

Qi Dou is with the Department of Computer Science and Engineering, The Chinese University of Hong Kong, Hong Kong (e-mail: qdou@cse.cuhk.edu.hk).

Pieter Abbeel is with the University of California at Berkeley, Berkeley, CA 94720 USA (e-mail: pabbeel@berkeley.edu).

This article has supplementary downloadable material available at https://doi.org/10.1109/TRO.2024.3508932, provided by the authors.

Digital Object Identifier 10.1109/TRO.2024.3508932

***Index Terms*—Grasping and manipulation, proprioception, robotic hand, soft actuation, soft robotics.**

I. Introduction

ROBOTIC manipulation systems have emerged as promising solutions to address labor shortages, reduce costs, and collaborate in daily living tasks. Despite numerous advancements in robotic grasping, a persistent gap remains between human and robotic performance in dexterous manipulation [1]. Humans possess an inherent skill for fine in-hand manipulation [see Fig. 1(a)], utilizing dexterous interactions both intrafinger (in-finger) and between fingers and environment (finger–environment) for various daily tasks. Replicating these fine in-hand manipulation skills in robotics remains a formidable challenge [2], necessitating innovative approaches to bridge existing disparities from robot design, sensing, and control perspectives.

Over the past few decades, research has focused on two main directions in robotic hand development. One direction involves anthropomorphic robotic hands with high dexterity and general functionality, which come with high complexity [3], [4]. The other direction focuses on the simpler grippers with straightforward designs tailored for specific and desired tasks. In recent years, dexterous anthropomorphic hands have become available for a wider range of manipulation tasks, thanks to advancements in compliant mechanisms [5], [6], [7], [8] and learning-based algorithms [9], [10], [11]. These improvements simplify the uncertainties of complex physical interactions during manipulation. However, previous efforts have demonstrated that achieving a delicate balance between control complexity, compliance, dexterity, motion accuracy, and system complexity remains both desirable and challenging.

To address the intricate balance required for robotic in-hand manipulation, this study introduces the dexterous and compliant (DexCo) hand system utilizing soft hydraulic actuation. It covers hand design, actuation, modeling, and control strategies [see Fig. 1(b)]. Rigorous experiments were carried out to characterize the system and offer design customization recommendations. The results demonstrate that our DexCo hand successfully achieves fine in-hand manipulation tasks, showcasing its potential as a solution for robotic dexterous in-hand manipulation toward the human level [see Fig. 1(c)]. The contribution of this work is summarized as follows.

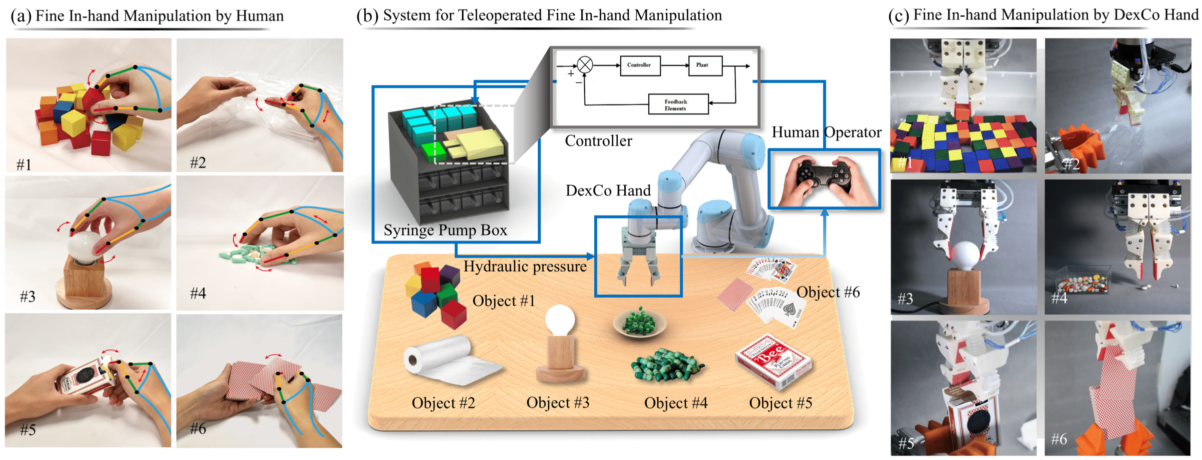

Fig. 1. (a) Typical fine in-hand manipulation tasks performed by human: (#1) cluttered bin picking; (#2) opening a sealed plastic bag; (#3) screwing on and off light bulb; (#4) picking and sorting granular objects; (#5) opening card box and extracting cards from card box; and (#6) counting cards. (b) Teleoperated robotic system to perform various grasping and manipulation tasks. (c) Human-inspired fine in-hand manipulation tasks realized by the proposed DexCo hand.

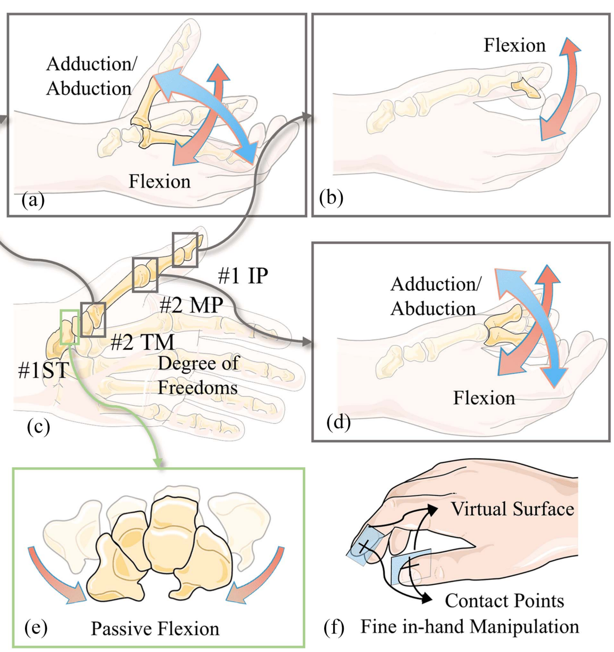

Fig. 2. (a) Two active DoFs at trapeziometacarpal (TM) joint. (b) One active DoF at interphalangeal (IP) joint. (c) DoFs for human thumb. (d) Two active DoFs at metacarpophalangeal (MP) joint. (e) One passive DoF at the metacarpal joint. This DoF initiates the flexion motion of thumb. (f) Virtual contact surface and contact points when human perform in-finger manipulation.

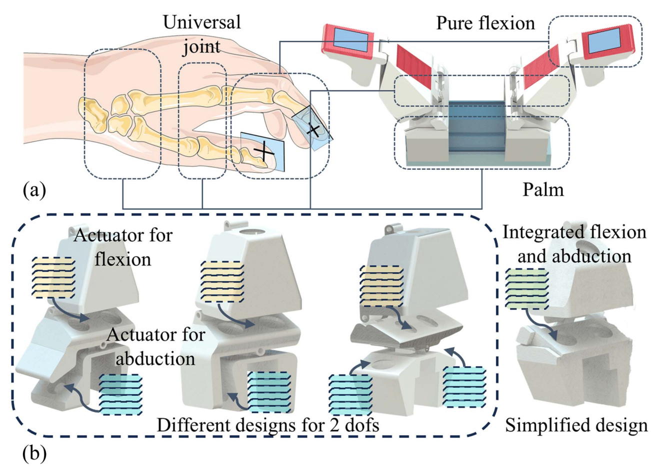

Fig. 3. Mapping from human hand to robotics hand. (a) Corresponding relationship between each part of the human hand and the robotic hand. (b) Different mechanical realization of adduction/abduction freedom.

TABLE I
MAJOR PARAMETERS AND VARIABLES OF THE SS-ACTUATORS

Parameters	Values
Inner diameter: d_0(mm)	14
Initial outer diameter: D_0(mm)	22
Chamber wall thickness: t(mm)	0.2
Number of convolutions: N	6
Young's modulus (MPa)	87
Poisson's ratio	0.38
Inner diameter (mm)	d
Outer diameter (mm)	D
Chamber wall length (mm)	l_r
Initial height of one convolution (mm)	h_0
Height of one convolution (mm)	h
Initial volume of one convolution (mm^3)	V_0
Volume of one convolution (mm^3)	V
Pressure in soft actuator (MPa)	P

1) This article proposes DexCo Hand with anthropomorphic design consideration, integrating flexion, adduction/abduction, finger opposition, and palm dexterity for human-like in-hand manipulability [see Fig. 3(a)]. Benchmark experiments indicate that the grasp strength ranges from 20.14 to 38.24 N (see Table IV) and cycle times ranging from 1.02 to 2.04 s (see Table V).
2) It proposes the soft hydraulic actuation approach, crucial for controllable in-hand manipulation. This approach

TABLE II
TRANSFORMATION OF STIFFNESS AND COMPLIANCE OF CONTACT INTERFACE

Stiffness	$K_a = J_a^T K_q J_a$	$K_q = J_q^T K_f J_q$	$K_f = H^T K_{tr} H$	$H^T K_{tr} H = K_p$	${}_B^p J^T K_p {}_B^p J = K_b$
	ACTUATOR	**CONFIGURATION**	**CONTACT**	**CONTACT**	**OBJECT**
Compliance	$J_a C_a J_a^T = C_q$	$J_q C_q J_q^T = C_f$	$H C_f H^T = C_{tr}$	$C_{tr} = H C_p H^T$	$C_p = {}_B^P J_b {}_b^p J^T$

TABLE III
KINEMATICS AND CONTACT INTERFACE

Motion	$J_\theta \delta\theta = \delta x_f$ $(6 \times m)(m \times 1)(6 \times 1)$	$H\delta x_f = \delta x_{tr} = H\delta x$ $(n \times 6)(6 \times 1)$ $(n \times 1)(n \times 6)(6 \times 1)$	${}_B^P J \delta x_b = \delta x_p$ $(6 \times 6)(6 \times 1)(6 \times 1)$
	CONFIG	**CONTACT**	**OBJECT**
Force	$J_\theta^T f_f = \tau$ $(m \times 6)(6 \times 1)(m \times 1)$	$f_f = H^T f_{tr} = f_p$ $(6 \times 1)(6 \times n)$ $(n \times 1)(6 \times 1)$	${}_B^P J^T f_p = f_b$ $(6 \times 6)(6 \times 1)(6 \times 1)$

TABLE IV
GRASP STRENGTH OF DIFFERENT GRASP TYPES AND ARTIFACT SIZE DIMENSIONS

Grasp type	Artifact size (mm)	Avg total force (N)	Stdev (N)	95% confidence interval (N)
Power	40	27.16	1.97	[26.45, 27.87]
	55	26.31	2.30	[25.48, 27.14]
	70	24.10	1.76	[23.47, 24.73]
	85	24.83	1.77	[24.19, 25.47]
Pinch	35	20.14	1.55	[19.13, 19.99]
	60	21.31	2.08	[20.22, 22.40]
	85	22.40	0.87	[21.36, 23.43]
	110	29.26	1.88	[28.29, 30.23]
	120	38.24	2.70	[37.24, 39.24]

TABLE V
GRASP CYCLE FOR DIFFERENT GRASP TYPES AND ARTIFACT SIZE DIMENSIONS

Grasp type	Artifact size (mm)	Avg cycle time (s)	Stdev (s)	95% confidence interval (s)
Power	40	1.40	0.09	[1.37, 1.43]
	55	1.36	0.15	[1.30, 1.41]
	70	1.39	0.06	[1.37, 1.41]
	85	1.33	0.14	[1.28, 1.38]
Pinch	35	2.04	0.10	[2.00, 2.07]
	60	1.59	0.04	[1.57, 1.60]
	85	1.41	0.05	[1.40, 1.43]
	110	1.13	0.08	[1.10, 1.16]
	120	1.02	0.06	[1.00, 1.04]

effectively balances robotic hand control complexity, dexterity, compliance, and accuracy, providing a comprehensive solution.

3) It extends DexCo hand dexterity and compliance models to a hand simulator. The model, incorporating hydrostatic force analysis, effectively illustrates hand joint motion and compliance. A dedicated ROS package has been developed to simulate the DexCo hand, showcasing its capabilities and development in a virtual environment.
4) It designs dedicated velocity and position teleoperation controllers for executing real-world physical manipulation tasks effectively.
5) It proposes a twist strength benchmark and comprehensive hand evaluation, including fundamental assessments and real manipulation tasks, to enhance robotic fine in-hand manipulation toward human-comparable dexterity and performance levels.

The rest of this article is organized as follows. Section II presents a thorough review of related works on dexterous hands and manipulation, emphasizing our unique contributions. Section III elaborates on the innovative structure and design of the dexterous hand, utilizing soft hydraulic actuation with dedicated modeling. In Section IV, this article develops models to quantify manipulability and compliance of the hand and provides a tool to evaluate and enhance the design efficiently. Dedicated fundamental experimental characterizations are presented in Section V, followed by Section VI, which demonstrates the hand's fine in-hand manipulation capabilities. Finally, Section VII concludes this article. The appendixes provide details on calibration, simulator development, and controller design.

II. RELATED WORKS

This section is dedicated to reviewing related work in three key aspects of in-hand manipulation: design, actuation, and sensing. By summarizing existing approaches, we aim to highlight the differences and innovations of our approach in addressing current challenges.

A. Hand Design

The structural configurations of robotic hands encompass various elements such as the number of fingers, degrees of freedom (DoFs) of the fingers, finger layout, topological structure of links, joint types, and structural materials. These variations, further cooperating with sensing, control, and interaction, impact the complexity of the robotic hand. Despite its simplicity, the two-finger parallel gripper remains widely used, featuring two single-segment fingers with a single DoF. Movement is achieved through a linear guide rail or a rotary linkage mechanism. Another variant employs rotational joints for object envelopment and securing, with optimizations in topological structure by Rodriguez and Mason [12], [13]. Soft robotics has introduced a soft material counterpart of the two-finger gripper [14], with attempts to enhance variable stiffness using rigid substances [15], [16], [17]. Overall, two-finger grippers excel in single tasks like pinch grasping [18] and power grasping [19], [20], [21], performing manipulation such as pushing [22], [23], [24], and extrinsic dexterity [25], [26], [27] utilizing environment.

Increasing the number of fingers and joints enhances task diversity [28], [29], [30] and performs well in specific tasks [31], such as sliding, rotation, pushing, extrinsic dexterity, and caging. Mason et al. [31] proposed a stable multifingered hand with single rotational DoFs per finger. Multijointed two-fingered hands strike a balance between complexity, reliability, and task diversity, such as the Velo gripper [32], which uses revolute joints with a pulley system to adaptively grasp objects with pinch-power switching capability. Other designs, such as Yoon et al.'s linkage mechanism [33] and Kim et al.'s belt and linkage structures [34], offer adaptability to different grasping surfaces and switchable grasping modes. Roller joints introduced by Yuan et al. [35], [36] achieve dexterity surpassing that of the human hand in specific tasks. The Model W hand by Bircher et al. [37] introduces translational freedom to the palm, enhancing manipulation through caging. On the other hand, the soft counterparts, such as the SDM hand [38] and its derivatives [39], [40], [41], [42], [43], [44], [45], [46], [47], feature compliance from soft structures at joints, enhancing robustness in unstructured environments. The authors previously proposed that the pneumatic soft-rigid hybrid hand offers improved grasping adaptiveness and robustness [48]. By incorporating lateral DoFs [49], this solution also demonstrates early lateral manipulation capabilities and lateral compliance. Furthermore, Xia et al. [50] demonstrate an extension of pneumatic joints integrated with a tendon-driven approach. While gas-tendon coupled actuation offers tendon-driven control and gas-driven compliance, it faces limitations: redundant system design, challenging tendon layout, synchronization issues, interference, and reduced control precision over time. These challenges, including accuracy, compliance, control complexity, and quantifiable modeling, continue to affect pneumatic soft-rigid hybrid joints, limiting their utilization in more complex manipulation tasks.

Early anthropomorphic hands, such as the Salisbury hand [51], modular hand [52], Pisa/IIT hand [53], [54], and others [55], [56], [57], were designed to perform general manipulation. While recent learning methods, including reinforcement learning and imitation learning, have improved task diversity and robustness, challenges related to actuation, structure, control complexity, and hardware portability persist. These issues hinder the ability to obtain training data, define tasks, and bridge the sim-to-real gap, limiting algorithmic capabilities and exploration of task diversity. Soft multisegment hands [58], [59] and soft anthropomorphic hands, such as the RBO Hand [21], [52], tactile hand [60], and BCL-26 [8], enhance environmental adaptability and reduce control complexity. However, current designs still face challenges, such as complex control, difficulty obtaining effective training data, lack of simulation capabilities, reliance on hardcoded movements, and limited dexterity and precision. As a result, compliant hands remain effective for adaptive grasping but struggle to demonstrate clear advantages in more complex manipulation tasks, like fine manipulation, where balancing control complexity, dexterity, compliance, and accuracy is still a challenge.

B. Hand Actuation

Robotic hand actuation methods are primarily motor-driven or fluid-driven. Motor-driven methods include gears, linkages, slides, or cable drives [34], [35], [37], [61]. Cable-driven actuation, popular in dexterous hands [32], [38], [51], [54], [62], offers a more compact structure, enabling higher DoFs, but introducing control complexity [63]. Fluid-driven actuation [64], including hydraulics and pneumatics, gains popularity in soft robotics [65], offering functional, compact, and lightweight grippers [66], [67], [68].

Actuation complexity can be classified as fully actuated or underactuated systems. Fully actuated systems have higher hardware and control complexity [69], [70], while underactuated systems simplify algorithms and control, facilitating diverse grasping and manipulation tasks [8], [28].

C. Hand Sensing

The position and force sensing of a dexterous hand greatly influence the reliability of algorithm development for these devices. Many proprioception schemes for dexterous hands rely on external methods, such as using cameras [71], [72], [73] or motion capture systems [28], [74], to obtain the posture of the dexterous hand. Internal sensing methods, such as servos [9], encoders, and magnetic encoders, can provide high-precision angle feedback. However, due to installation location and size constraints, the applicability of these internal sensing solutions is limited. For instance, they are not feasible for use with ball joints or flexible joints. Emerging sensing methods for soft robotics also offer new perspectives for dexterous hand proprioception. Odhner et al. [39] have used optical fiber to sense flexure at soft robotic joints, while Huang et al. [66] and Wang et al. [75], among others, have utilized flexible inductive sensors to provide feedback on linear and rotational movements, as well as spatial posture. Sundaram et al. [76] have employed custom magnetic fields to sense two degrees of rotational freedom. However, the main issues with these novel methods are accuracy, hysteresis, and durability.

III. DexCo Hand Design

This section introduces the design details of the DexCo hand, including anthropomorphic structure and kinematics, soft hydraulic actuation and modeling, and hand proprioception.

A. Structure and Kinematics

The dexterity and compliance of the human hand enable it to handle complex interactions and rich contacts [2], [77]. The thumb has six DoFs [as shown in Fig. 2(c)]. Starting from the fingertip, these are the interphalangeal (IP) joint [see Fig. 2(b)], the metacarpophalangeal (MP) joint [see Fig. 2(d)], the trapeziometacarpal (TM) joint [see Fig. 2(a)], and the scaphotrapezial (ST) joint [see Fig. 2(e)]. The ST joint is a passive DoF that provides an initial flexion movement when the thumb moves. The other five DoFs are active. The dual DoFs of the MP and TM joints arise from their saddle-shaped structure, which allows movements similar to a universal joint. For fine in-hand manipulation (including grasping), for which the human hand is particularly adept, the thumb and index finger need to have either direct or indirect contact, which can be abstracted

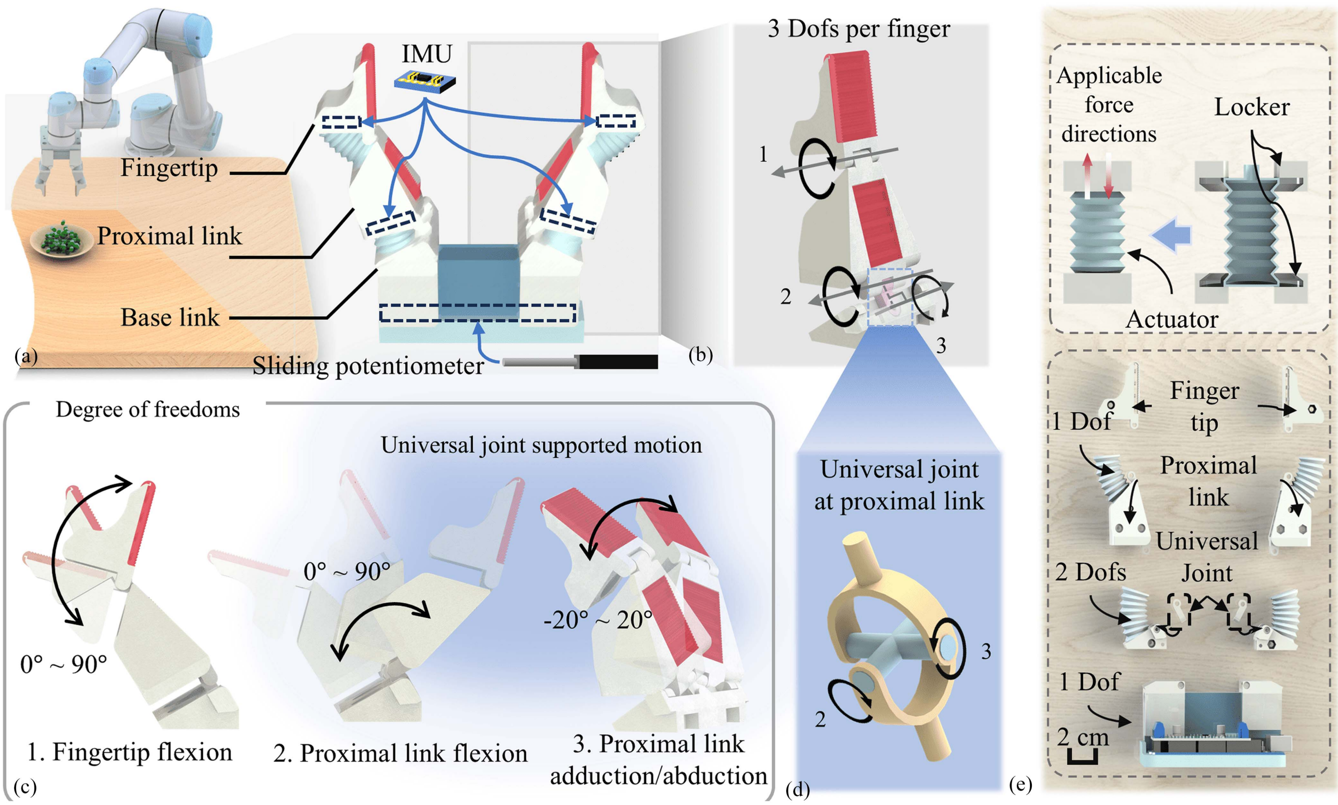

Fig. 4. (a) Front view of the DexCo Hand and the sensor installation positions. (b) Structure and three DoFs of the finger. (c) Finger motions generated from the three DoFs. (d) Universal joint connecting the proximal link and base link. (e) Assembly method for actuators and an exploded view of the DexCo Hand.

into a "contact point" and a "virtual surface" [see Fig. 2(f)]. Thus, three DoFs of the thumb are used to align the contact point, and the other two are used to align the virtual surface, as referenced in [78]. Overall, these six DoFs enable the thumb to flexibly adjust its orientation and position relative to the palm. In addition, the index finger of the human hand has two flexion DoFs near the fingertip and flexion, adduction/abduction DoFs at the base.

The intuitive direction is to imitate the functionality of the human index finger and thumb, achieving fine in-hand manipulation. To this end, we abstracted and mimicked three characteristics from the manipulation process between the thumb and index finger and then applied them to the two-fingered hand, as shown in Fig. 3(a). The first is the flexion motion, which is common in two-fingered hands. Flexion, whether in a single joint or multiple joints, provides the ability to grasp, as well as the capacity for manipulation skills like sliding, pushing, and caging. Another characteristic is the adduction/abduction movement of human fingers [see Fig. 3(b)]. This adduction/abduction movement is observable in all fingers. We noted that adduction/abduction movements are essential for performing certain tasks and can improve the efficiency and robustness of others. Without these movements, tasks may require wrist and arm movements, necessitating complex modeling and control. This indicates that adduction/abduction has the potential to significantly enhance the functionality and efficiency of robotic hands. The final feature is the large motion range of the thumb relative to the palm. This feature is derived from the high dexterity and suited skeleton length of the thumb. However, integrating all six DoFs into a single finger, even if passive, would increase the complexity of actuation and proprioception, leading to reduced reliability, as noted in [52]. Therefore, considering that two of the six DoFs help the thumb adjust the virtual surface, the opposition structure of the two-fingered hand can eliminate the dependence on these two DoFs. Furthermore, we ensure that each finger has three DoFs (two for flexion and one for adduction/abduction) to align the contact point [see Fig. 2(f)], which is fundamental for dexterity. In addition, we use one DoF in the palm to accommodate the thumb's ability to move across a wide range relative to the palm using multiple DoFs.

The DexCo hand, as shown in Fig. 4(a) and 4(e), features modular fingers. Each finger is composed of three links: the base, proximal, and fingertip link. These links encompass three DoFs, formed by two joints, as illustrated in Fig. 4(b). The joints consist of a two-DoF universal joint at the proximal end and a revolute joint at the fingertip. One rotational axis of the universal joint is parallel to the fingertip's rotational axis, enabling two independent DoFs for flexion movements. The other DoF of the universal joint, perpendicular to the flexion axis, facilitates adduction/abduction movements, as shown in Fig. 4(c) and 4(d). The use of the universal joint significantly reduces the complexity of the fingers in performing adduction/abduction movements. Other designs, as shown in Fig. 3(b), which continue to use traditional cascaded revolute joints, encounter several challenges. From a control perspective, multistage cascading introduces the maximum inertia at the proximal end, reducing

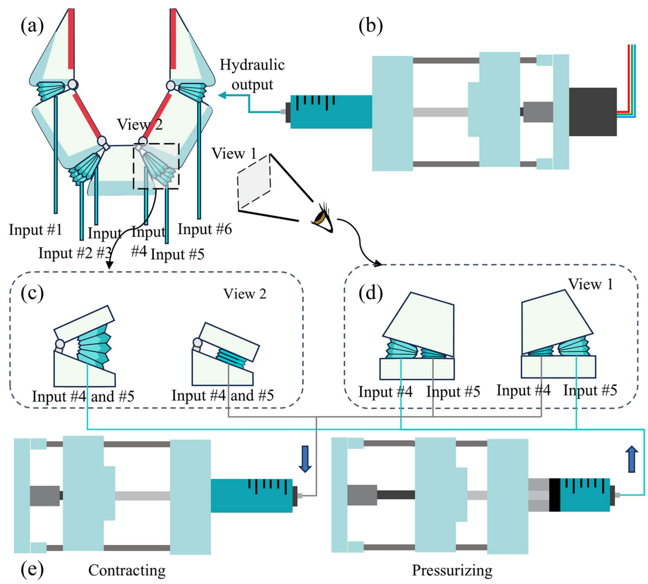

Fig. 5. Actuation mechanism. (a) Illustration of DexCo hand. (b) Hydraulic syringe pump. (c) The flexion motion from the front view. (d) The adduction/abduction motion from the side view. (e) Contracting and pressurizing mode for hydraulic syringe pump.

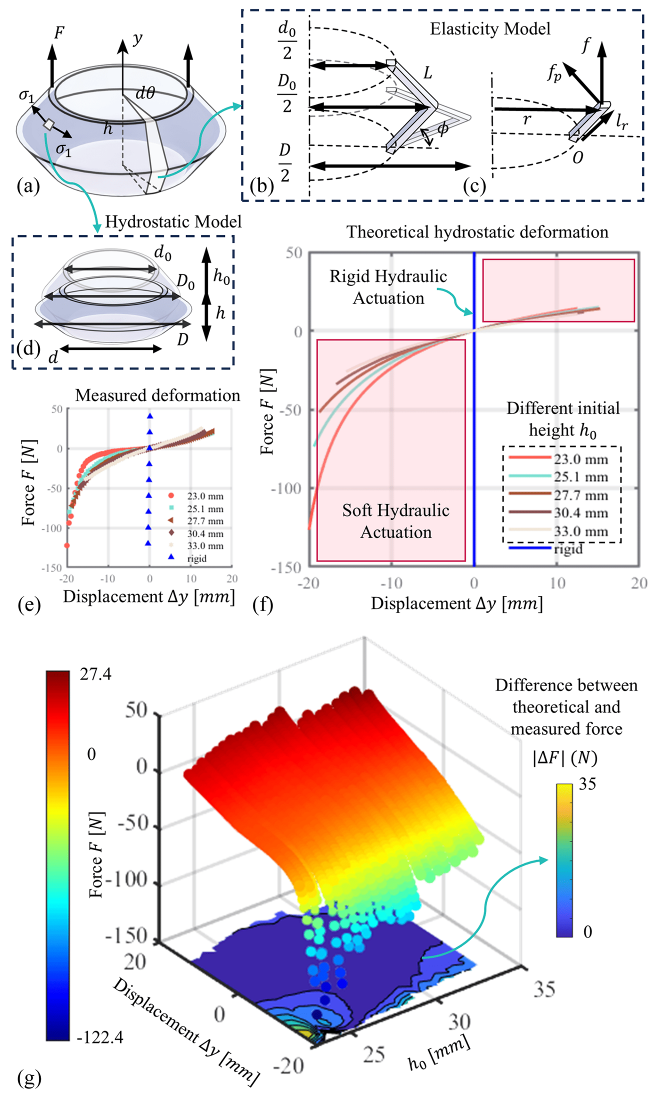

Fig. 6. (a) One convolution of the origami actuator. (b) and (c) are involved in the elastic force modeling. (b) shows a $d\theta$ section of the actuator and the geometric constraints used in elastic force analysis. (c) shows an infinitesimal element of the section. (d) Hydrostatic modeling based on a thin wall piece and the geometric constraints applied in hydrostatic modeling. (e) Measured deformation model. (f) Theoretical deformation model with an emphasis on the comparison between soft and rigid hydraulic actuation. (h) Full illustration of measured deformation and the difference with the theoretical model. The bottom contour shows the difference between measured and theoretical force.

control stability. In terms of kinematics, longer fingers generally decrease dexterity. From a sensing perspective, more actuators mean more sensors are needed, leading to a larger and more complex system. The range of motion for each joint is illustrated in Fig. 4(c). The fingertip rotational joint ranges from 0° to 90°. The universal joint's range of motion in the flexion direction extends from 0° to 90°, and in the adduction/abduction direction, it ranges from −20° to 20°.

These two modular fingers are mounted on a pneumatic slide that performs linear motion, which we refer to as the palm [see Fig. 4(e)]. The palm (SMC MHF2-12D2R) is pneumatically driven and can withstand a range of air pressures, supporting a relatively large gripping force (48 N). With two pneumatic inputs, the slide can control both stiffness and position. It has a travel distance of 60 mm, which provides significant dexterity for fine in-hand operations during experimental tasks. Observations from experiments suggest that increasing the slide's travel distance could further enhance operational dexterity.

B. Soft Hydraulic Actuation

The soft hydraulic actuation mechanism is a pivotal aspect of the proposed design, illustrated in Figs. 5 and 6, and seamlessly integrates dexterity and compliance into a compact form. The refined origami (Bellow type) actuators, showcased in Fig. 5(c)–5(e), exhibit excellent airtightness, durability, and a high expansion ratio, contributing to the effective driving of the revolute joint. The driving principles of the revolute joint have been extensively detailed in our previous work [48], [66], and [68].

Operating under hydrostatic pressure, this mechanism provides accuracy, local compliance, and bidirectional driving capabilities. The intrinsic properties of hydraulic actuation ensure accuracy and stability, while local compliance leverages the benefits of soft materials, creating a resilient interaction space and reducing the risk of hardware damage. Building on this mechanism, the integration of a universal joint closely replicates the dexterous base joint of a human finger [see Fig. 5(c) and 5(d)] with the simplest actuation. The base joint is actuated by a pair of hydraulic actuators through differential actuation. This innovative approach empowers the mechanical hand to achieve universal joint motion with minimal complexity and facilitates the easy embedding of proprioception. Collectively, these features enable the mechanical hand to replicate the functions of human thumbs and index fingers while optimizing the hardware structure to the greatest extent possible.

The design of the origami actuators revolves around two key aspects: customization of the actuator's behavior through design parameters and consideration of specific materials and fabrication methods based on functional requirements. Design parameters, outlined in Table I, focus on modifying the zig-zag origami characteristics. Adjusting the relative angle between two adjacent zig-zag features, for example, allows for the alteration of the actuator's initial length. Similarly, modifying the depth-to-diameter ratio influences the mechanical characteristics of the actuator during motion, while changing the number of origami layers directly impacts its expansion length.

In terms of fabrication, the actuator needs to meet the force output requirements of the dexterous hand, requiring a certain level of pressure resistance. Given the challenge of manufacturing small-scale, pressure-resistant, and airtight actuators, we selected blow molding as the preferred method. Polyethylene, chosen for its toughness and extensibility, serves as the material for blow molding. This choice ensures that the actuators can maintain thinness without compromising durability, even after undergoing repeated positive and negative pressure cycles and extreme position movements.

The origami actuator is hydraulically driven, as depicted in Fig. 5(b). On the one hand, in contrast to pneumatic actuators, which exhibit notable compressibility, hydraulic actuators offer higher stiffness during the interaction. For dexterous hand applications, lower stiffness is not always desirable, as it may require the introduction of a variable stiffness mechanism, thereby increasing system complexity and control challenges [49]. The higher stiffness of the hydraulic actuators ensures a proportional relationship between the volume of the liquid and the length of the actuator even under external forces. This characteristic facilitates the driving of the two DoFs in the configuration space of the universal joint: simultaneous elongation or shortening of both actuators induces flexion, while differential elongation and shortening result in adduction/abduction movements of the universal joint.

On the other hand, conventional rigid hydraulic actuation bears similarity to motor actuation, lacking inherent compliance and necessitating active force control for the interaction, as illustrated in Fig. 6(a). In contradistinction, soft hydraulic actuation integrates the advantageous features of a soft actuator and hydraulic actuation, concurrently achieving forceful output, inherent compliance, and optimal actuation efficiency, as depicted in Fig. 6(f). Here, we aim to obtain a deformation model for the hydraulic actuators, i.e.,

$$F \triangleq g\left(h_0, \Delta y\right) = F_e + F_h \tag{1}$$

where h_0 represents the initial height of the actuators, F_e is the elastic force that is always used in pneumatic actuation modeling [66], [79], and F_h represents the hydrostatic force. We tune the initial height by hydraulically pressurizing the actuators. This model describes the relationship between force F and linear deformation Δy under a certain initial height of the actuator. The main parameters and variables involved in the derivation are shown in Table I.

1) Elastic Force Modeling: Wang and Wang [79] demonstrated the elastic force of a hollow origami tube under external force, while our model further considered the actuator's internal pressure force. This internal pressure force becomes prominent when the actuation media changes from low density to high density.

First, as the upper and lower halves of a single-convolution origami actuator are symmetrical [see Fig. 6(a)], their strains are identical. Based on Castigliano's theorem, we can derive

$$\delta y = 2\frac{\partial U}{\partial f} = 2\int_{d/2}^{D/2} \frac{M}{EI}\frac{\partial M}{\partial f} dr \tag{2}$$

where U is the strain energy, f is the force on an infinitesimal element of the actuator [see Fig. 6(b)], i.e. $f = F_e.\ \frac{d\theta}{2\pi}$, δy is the displacement of one convolution of the actuator, M is the torque at the current position r, E is Young's modulus, and I is the moment of inertia at the current infinitesimal element, i.e., $I = \frac{t^3}{12(1-\mu^2)} r d\theta$.

The torque M and its partial derivative are

$$M = \underbrace{f\left(r - \frac{d}{2}\right)}_{M_f} + \underbrace{Pd\theta\left(\frac{1}{3}\cos\phi \cdot l_r^3 + \frac{d}{4}l_r^2\right)}_{M_{f_p}} \tag{3}$$

$$\frac{\partial M}{\partial f} = r - \frac{d}{2} + \frac{8}{d^2}\left(\frac{1}{3}\cos\phi \cdot l_r^3 + \frac{d}{4}l_r^2\right) \tag{4}$$

where r is the distance from the actuator wall to the central axis, P is the internal pressure of the fluid, and $l_r = \frac{r-d/2}{\cos\phi}$. In (3), the left-hand side $f(r - \frac{d}{2})$, M_f, is the torque produced by force f, and the right-hand side $Pd\theta(\frac{1}{3}\cos\phi \cdot l_r^3 + \frac{d}{4}l_r^2)$, M_{f_p}, is the torque on the actuator's wall produced by internal pressure [see Fig. 6(c)], The pressure torque is obtained through the integral of pressure force along the chamber length, $\int_0^{l_r} Pl.\ yd\theta dl$, where l is the distance from O along the actuator's wall. Substituting (3) and (4) into (2), we can derive the function $F_e(h_0, \Delta y, D)$ by integrating the polynomial equation (2).

On the other hand, during actuator deformation, the geometric constraints between Δy, D, and d are based on the constant liquid volume. However, for simplification, we make the following assumption for the geometric constraint.

Assumption 1: The length of the actuator's wall L is constant, i.e., $L \triangleq \sqrt{(\frac{D_0-d_0}{2})^2 + (\frac{h_0}{2})^2}$, and the inner diameter is assumed to be constant, i.e., $d \triangleq d_0$.

Based on Assumption 1, we derive

$$D = d + \sqrt{h_0^2 + (D_0 - d)^2 - \left(\frac{\Delta y}{N} + h_0\right)^2} \tag{5}$$

where d_0 is assumed constant, h is the height of one convolution of the actuator, and D_0 is the initial outer diameter. Combining (2)–(5), the elastic force model $F_e(h_0, \Delta y)$ is attained, whose range is within -0.5 to 0.15 N. The force generated from the elastic force in these thin-walled soft actuators is rather small. Therefore, when effecting, hydrostatic force plays a vital role in interaction.

2) Hydrostatic Force Modeling: The hydrostatic force is also generated from the elastic deformation of the soft actuator. However, the elastic force results from the elastic deformation in the axial direction due to the compression or extension of the soft actuator, which could be referred to as a spring [see Fig. 6(b)].

The hydrostatic force is generated from the elastic deformation on the radial direction in the compression or extension phase [see Fig. 6(d)], which could be referred to as blowing a balloon. To attain the hydrostatic pressure, we make the geometric constraint.

Assumption 2: Under an initial height of the soft actuator h_0, the volume of water is constant during the motion phase, i.e., $V = V_0 \triangleq$ constant.

Based on Assumption 2, we have the geometric constraint

$$\begin{cases} V_0 = \frac{\pi h_0}{3}\left[\left(\frac{D_0}{2}\right)^2 + \left(\frac{D_0}{2}\right)^2 + \frac{D_0 d_0}{4}\right] \\ V = \frac{\pi h}{3}\left[\left(\frac{D}{2}\right)^2 + \left(\frac{D}{2}\right)^2 + \frac{Dd}{4}\right] \\ V = V_0 \end{cases} \tag{6}$$

where variables are shown in Table I. To derive the deformation in the radial direction, we compute the radial strain based on the thin-walled theory. First, as shown in Fig. 6(a), stress σ_1 is attained based on the axial profile

$$\sigma_1 = \frac{Pr}{t} \tag{7}$$

where r represents the radius at height y. Then, according to the generalized Hooker's law

$$\varepsilon_1 = \frac{\sigma_1}{E} = \frac{\Delta_1}{2\pi r} \tag{8}$$

where Δ_1 is the difference of the circumference under the stress and ε_1 represents the strain on the circumference. Therefore, based on (7) and (8), we attain the inner diameter and outer diameter under pressure P

$$\begin{cases} d = d_0 + \frac{2P}{Et} \cdot \left(\frac{d_0}{2}\right)^2 \\ D = D_0 + \frac{2P}{Et} \cdot \left(\frac{D_0}{2}\right)^2 \end{cases} \tag{9}$$

where $P \triangleq -\frac{4}{\pi d_0^2} F_h$.

Incorporating (9) into (6), we obtain the solution, i.e., $F_h = F_h(h_0, \Delta y)$, by solving a quadratic equation. As $F_h \gg F_e$, we have $F \approx F_h$. These results are presented in Fig. 6(e)–6(h), illustrating the effectiveness of soft hydraulic actuation, which relies on the hydrostatic force within soft materials. Compared to soft actuation, rigid hydraulic actuation, as shown in Fig. 6(f), has a significantly higher theoretical stiffness, a claim supported by the measured forces depicted in Fig. 6(e). The capabilities of soft hydraulic actuation are showcased in Fig. 6(f), demonstrating its ability to achieve on-demand compliance while providing adequate force output. Fig. 6(h) offers a comprehensive view of the measured forces, highlighting the force discrepancies between actual measurements and theoretical predictions at the bottom contour of the graph. Most areas within this contour display slight differences, affirming the accuracy of the hydrostatic analysis. However, a notable deviation occurs at the corners, attributed to unforeseen radial deformations.

Finally, the actuation of the hand is divided into two integral components: origami actuators seamlessly integrated into the hand and a syringe pump system situated at the back end, as illustrated in Fig. 5(a) and 5(b). Each origami actuator is equipped with a syringe pump as its driver. The syringe pump comprises a syringe, a stepper motor, a motor driver, and a magnetic encoder. The syringe is directly linked to the origami actuator, propelling its movement. When the volume inside the syringe is compressed, the origami actuator elongates; conversely, as the volume increases, the origami actuator shortens. This actuation method, referred to as direct pumping in [80], allows the syringe to utilize volumes ranging from 10 to 250 mL, precisely matching the volume of the origami actuator. To achieve high-speed actuation and substantial output force, a 57-stepper motor is chosen as the driver for the syringe pumps. The 57-stepper motor can efficiently drive a 250-mL syringe at high speeds. The synchronization of multiple stepper motors is accomplished through the IIC bus in conjunction with a microcontroller. This approach has successfully achieved low-latency synchronous movement within eight stepper motors, meeting the stringent requirements for synchronized control of multiple DoFs essential for the dexterous hand in this study. In addition, magnetic encoders provide high-precision feedback on the position of the stepper motors, facilitating closed-loop control of the syringe pumps.

C. DexCo Hand Proprioception

The proprioception system of the DexCo hand is primarily dedicated to sensing joint angles, which predominantly incorporates two types of sensors: a linear sliding potentiometer and an inertial measurement unit (IMU). The linear potentiometer is positioned at the palm joint, providing accurate feedback on the distance of the hand's opening and closing. On the other hand, the IMU is fixed to the proximal and fingertip links of the fingers, offering feedback on the revolute joints. Commercially available IMUs often consist of various microelectromechanical systems (MEMS) integrated chips, encompassing a three-axis accelerometer, a three-axis gyroscope, a three-axis magnetometer, and other measurement units such as barometers and thermometers for compensating drifts like temperature drift. This integration facilitates the convenient incorporation of the IMU into small spaces, such as within a finger, while still providing multiaxis rotational information.

The DexCo hand employs a commercially available MEMS IMU (ICM-20948, TDK InvenSense), a nine-axis IMU integrating accelerometers, gyroscopes, and magnetometers. To obtain the angle of the fingertip, the difference between the readings from the fingertip IMU and the proximal IMU is directly calculated. As the roll and pitch angles exhibit minimal drift, we align the x-axis of both IMUs parallel to the rotational axis of the fingertip, which not only reduces computational demands but also ensures minimal drift.

For acquiring the dual-axis angles of the universal joint, calculations are based on the known palm posture and Euler angles from the proximal IMU. Taking one finger as an example, the configuration space includes q_2, q_3, and q_4 (as shown in Fig. 7, configuration space is corresponding to each frame S_i). The angle of the fingertip, q_4, can be obtained by taking the difference between the corresponding angles from two IMUs, while the universal joint angles q_2 and q_3 are derived from the

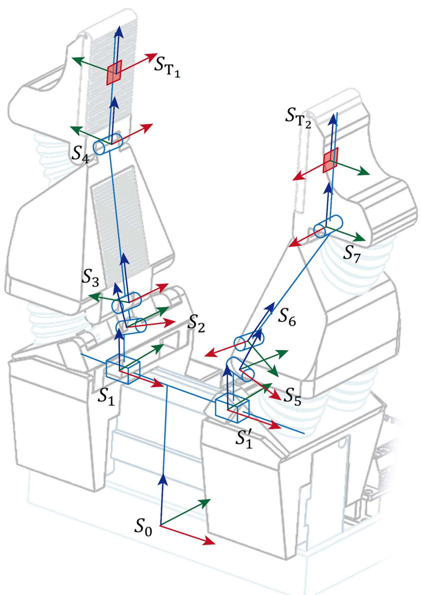

Fig. 7. Kinematic structure of the DexCo hand.

rotations in the configuration space as follows:

$$\begin{cases} R_y\left(-\frac{\pi}{6}\right) R_x\left(q_2\right) R_z\left(\frac{\pi}{2}\right) R_x\left(q_3\right) = {}^0R_3 \\ R_y\left(\frac{\pi}{6}\right) R_x\left(q_5\right) R_z\left(-\frac{\pi}{2}\right) R_x\left(q_6\right) = {}^0R_6. \end{cases} \tag{10}$$

Since the base of the hand is fixed to the end of the robotic arm, the posture of the palm base is known. By utilizing the IMU on the proximal link and the posture of the palm, we can obtain the rotation matrix ${}^0R_2$ of the proximal link relative to the base. $R_x(q_2)R_z(\frac{\pi}{2})R_x(q_3)$ in (10) represents the rotation matrix for the XZX Euler angles. Thus, we can determine the angles of the universal joint through (10). Unfortunately, the IMU can only provide stable feedback for angular data. Positional data, derived through the integration of accelerometer readings, suffer from significant drift issues. If not for this limitation, it would have been possible to determine the width of the palm using the two proximal IMUs.

IV. DexCo Hand Modeling

This section explores DexCo hand modeling, emphasizing manipulability and compliance as crucial metrics for quantitatively evaluating hand manipulation performance, reflecting the two key distinctive performance indices of the DexCo hand.

A. Dexterity and Manipulability Modeling

This section discusses the dexterity of the DexCo hand from two kinematic perspectives: the manipulability of a single finger and the manipulability of the entire hand. The manipulability of a single finger primarily considers two aspects. First, from the perspective of symmetry, since the three DoFs of the two fingers are symmetrical, the forces acting on the object (vector field) [62] or the manipulability in space can be regarded as the superposition of two identical fields. Second, from the principle of minimization, if the DexCo hand is viewed as comprising one three-DoF finger and one four-DoF finger (including the palm DoF), the manipulability of the configuration is determined by the finger with fewer DoFs, i.e., $\sigma(\chi) = \min(\sigma(\chi_1), \sigma(\chi_2))$. On the other hand, the manipulability of the entire hand considers all seven DoFs, where $S_{\mathrm{T}1}$ is set as the reference frame, and $S_{\mathrm{T}2}$ as the operating frame (see Fig. 7).

Considering the manipulability of a single finger, as previously mentioned, the homogeneous transformation matrix for the single finger with three DoFs is represented as

$${}^0T_{\mathrm{T}_1} = {}^0T_1{}^1T_2{}^2T_3{}^3T_4{}^4T_{\mathrm{T}_1} := \begin{bmatrix} {}^0R_{\mathrm{T}_1} & {}^0p_{\mathrm{T}_1} \\ 0 & 1 \end{bmatrix} \tag{11}$$

where ${}^0R_{\mathrm{T}_1} \in \Re^{3\times3}$ denotes the rotation matrix from the frame S_0 to the end-effector frame S_{T_1}, and ${}^0p_{\mathrm{T}_1} \in \Re^3$ represents the translation from S_0 to S_{T_1}. We focus on translational manipulability in this analysis. Meanwhile, we fix q_1 as constant in matrix ${}^0T_{\mathrm{T}_1}$, which indicates no movement in the palm. Consequently, the configuration space is defined as $q = [q_2, q_3, q_4]^T \in \Re^3$. The Jacobian matrix is

$$J(q) = \frac{\partial p}{\partial q} \in \Re^{3\times3}. \tag{12}$$

Excluding q_1 in the analysis of manipulability serves two purposes. On the one hand, it eliminates the translational redundancy in Cartesian space, thus simplifying the Jacobian matrix analysis. On the other hand, q_1 does not affect the manipulability metric σ_1: the redundancy of q_1 is equivalent to a translational superposition in the manipulability cloud of q, as shown in Fig. 8(c). Therefore, it is reasonable to analyze only the three DoFs for DexCo hand.

According to [81] and [82], the manipulability of a single serial mechanism can be defined as the inverse condition number of the Jacobian matrix in the entire workspace

$$\sigma_1(J) = \frac{1}{\mathrm{cond}(J(q))} = \frac{s_{\min}}{s_{\max}} \tag{13}$$

or the product of the eigenvalues of the Jacobian matrix

$$\sigma_2(J) = \sqrt{\det\left(J(q)\cdot J(q)^T\right)} = \sqrt{s_1 s_2 \ldots s_n} \tag{14}$$

where s_i is the eigenvalue of the matric $(J \cdot J^T)$, and $s_{\min}$ and $s_{\max}$ are the minimum and maximum eigenvalues, respectively. These two manipulability metrics measure different features. σ_1 represents the ratio of the shortest to the longest axis of the manipulability ellipsoid (as detailed in Appendix B). A smaller condition number, resulting in a larger value of σ_1, indicates that the manipulability ellipsoid is closer to a sphere. This implies that the motion of the end-effector caused by joint movements is more uniform in space. On the other hand, σ_2 represents the product of the semiaxes of the manipulability ellipsoid and thus is proportional to the volume of the ellipsoid. A larger value of σ_2 signifies a larger volume of the manipulability ellipsoid. Both metrics are better when larger.

The manipulability of a single finger is shown in Fig. 8(a)–8(d), where the logarithm of the condition number is normalized for better visualization. Configurations near the upper boundary generally have larger Jacobian matrix condition numbers, indicating lower manipulability. Manipulability ellipsoids for each configuration are depicted in Fig. 8(a) and 8(d). More

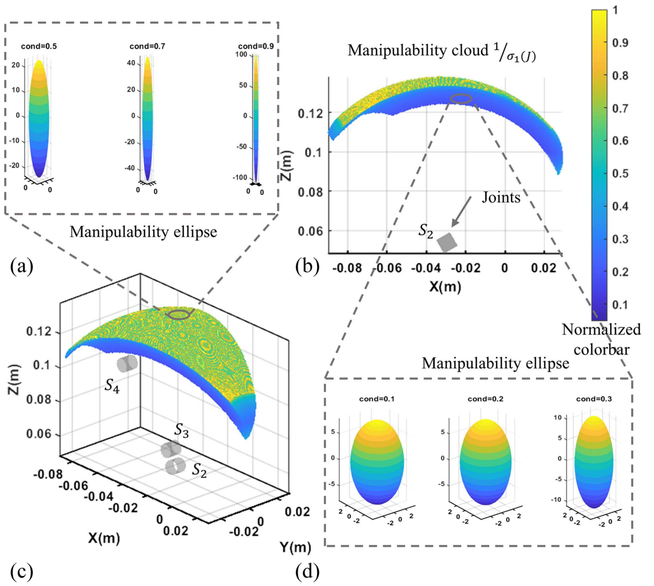

Fig. 8. Manipulability analysis and compliance analysis of a single finger. (a) Manipulability ellipse at the upper boundary of the Cartesian working space. (b) View of manipulability cloud from the xz plane. The color bar is applied to (b), (c), (e), and (g). (c) Manipulability cloud of a single finger. The upper boundary has a larger singularity; therefore, it has a lower manipulability. (d) Manipulability ellipse below the upper boundary of the Cartesian working space. As a lower value means higher manipulability, the blue area has a better manipulability under the singularity metric. (e) Compliance cloud in Cartesian space. The value at each point is attained based on the volume metric. (f) Compliance ellipse at the extremum. (g) Compliance cloud in Cartesian space. The value at each point is attained based on the condition number metric. Take the logarithm of the condition number and then normalize the result.

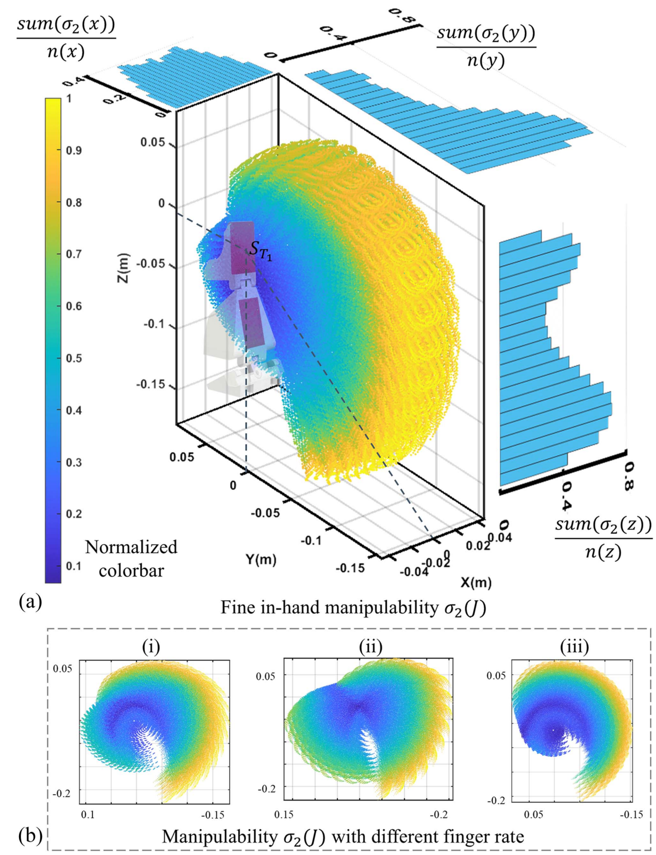

Fig. 9. Manipulability analysis of the whole hand. (a) Reference frame is selected as S_{T1}. The operating frame is selected as S_{T2}. The 3-D view shows in-finger manipulability without considering obstacles. Other plots show the distribution of the average manipulability on three axis. (b) YZ plane view of different finger linkage lengths: (i) length ratio alike a human finger (1:1); (ii) longer length on the middle link (ratio 1:5); and (iii) longer length on the fingertip link (ratio 5:1).

consistent motion in Cartesian space corresponds to ellipsoids with axes of similar lengths. Near singularities [see Fig. 8(a)], ellipsoids elongate, whereas in the center and lower part, they are more regular [see Fig. 8(d)]. If palm translation is included, the cloud can be seen as Fig. 8(b) shifted along the x-axis. When the left and right fingers contact, their interaction supports fine in-hand manipulation. The manipulability metric σ_2 shows similar trends as σ_1. Another unresolved question mentioned in [78] is that the flexion of the index finger significantly reduces its range of adduction/abduction motion. This aligns with the results shown in Fig. 8(c), where an increased flexion angle reduces the range of motion for S_{T_1} along the y-axis, resulting in a sector shape. Therefore, the issue raised in [78] is attributed to kinematic factors rather than the muscle structure of the index finger limiting the range of motion.

The overall hand manipulability, σ_2, normalized for visualization, is shown in Fig. 9. The Jacobian matrix here is $J \in \Re^{3\times7}$, taking into account the motion of all seven joints (two at the palm is regarded as equivalent) but only considers the translational space for visualization. The manipulability of the entire hand is the greatest at 1. It is worth noting that outside the yellow region, there should be a very thin layer with blue, which indicates the reduced manipulability at the task space boundary. In the σ_2 manipulability cloud, 80% of the manipulability is concentrated in the range of 0.2–0.5. In addition, Fig. 9(a) includes three graphs showing the mean distribution of manipulability. These graphs separately depict the distribution of manipulability along the x, y, and z axes. Each axis is divided into 20 intervals, with n representing the number of sampling points in each interval.

By changing the ratio of link lengths $S_4S_{T_1} : S_3S_4$, we attain different workspace and manipulability distributions [see Fig. 9(b)]. We designed the dimensions of the DexCo hand based on experience, resulting in a workspace and manipulability similar to the human finger ratio [see Fig. 9(b-i)]. Furthermore, based on the workspace and manipulability, we should be able to customize the DexCo hand for specific tasks in the future [see Fig. 9(b-i) and (b-iii)].

B. DexCo Hand Compliance Modeling

As the origami actuator uses soft materials as its shell, it undergoes local deformation under external force. The force–deformation relationship of the origami actuator, $F = g(h_0, \Delta y)$, has been analyzed in the actuation section. In the grasping and manipulation processes, this deformation brings compliance to the DexCo hand. Compliance has been proven to simplify control in interaction tasks, as referenced in [83]. End-effector tasks, particularly fine in-hand manipulation, involve complex contact and interaction, thus emphasizing the importance of the compliance analysis. Referring to [84], the relationship between the motion transformation and force transformation of the robotic hand is shown in Table II. In the table, q represents the displacement in the configuration space of the fingers; x_f, x_{tr}, x_p, and x_b are displacements in the Cartesian space: x_f is the coordinate at the contact point on the hand, x_{tr} is the part of the motion transmitted, x_p is the coordinate at the contact point on the object, and x_b is the selected external coordinate system. H is the selection matrix, and ${}^P_B J$ is the coordinate transformation from frame $\{P\}$ to frame $\{B\}$.

K is the stiffness matrix under different spaces, including the actuation space a, configuration space q, cartesian space f, p, b, and transmission space tr. The assumption behind using the stiffness matrix is that the elastic force is assumed to be affine, while the stiffness could be variable or nonlinear. To estimate the stiffness of an object held by the hand or the joint stiffness, we need to get the transformation from the actuator to the object or from the object back to the actuator, as shown in Table II. In Table II, the derivation of each column is similar. Therefore, we take the derivation process of the second column as an example, which transforms the stiffness matrix between the actuation space and the configuration space.

The same as the CONFIG column in Table III, we attain the kinematics relation between the action space and configuration space

$$\begin{cases} \delta q = J_a \delta a \\ J_a^T \tau = f_a \end{cases} \tag{15}$$

where δa is the displacement of the actuator in the actuation space, δq is the displacement in the configuration space, f_a denotes applied force by the origami actuator, and τ is the torque at each joint. The stiffness equations in the actuation space are

$$\begin{cases} f_a = K_a \delta a \\ C_a f_a = \delta a. \end{cases} \tag{16}$$

Combining (15) and (16) yields the transformation of the stiffness and compliance matrices between the actuation space and the configuration space, as shown in the second column of Table II. The transformation of the stiffness and compliance matrices between other spaces can also be obtained with the same method, based on the kinematics relation in Table III.

The compliance analysis, similar to the manipulability analysis, is based on the three-DoF fingers of the DexCo Hand. The metrics σ_1 and σ_2 are used to measure the stiffness of the fingers in space. The examples to showcase compliance analysis and the usage of stiffness transformation are separated into two cases. On the one hand, we present the object stiffness in holding. On the other hand, we propose a simulator for the DexCo hand simulation in Appendix D, which makes use of the stiffness transformation in the second column of Table II.

To determine the stiffness of the object held by the finger, K_b, the first step involves obtaining K_a and J_a. For K_a, we can assume

$$K_a = \mathrm{diag}([-1, -1, -1, -1]) \in \mathfrak{R}^{4\times 4}. \tag{17}$$

This assumption simplifies the analysis, as the specific stiffness characteristics are not the primary focus of this analysis. In addition, for J_a, we can also assume that

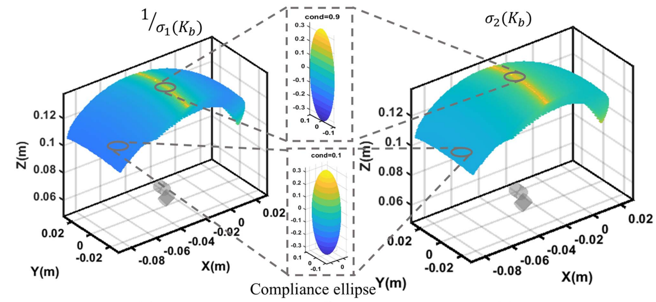

(a) (b) (c)

Fig. 10. Manipulability analysis and compliance analysis of a single finger. (a) Compliance cloud in Cartesian space. The value at each point is attained based on the volume metric. (b) Compliance ellipse at the extremum. (c) Compliance cloud in Cartesian space. The value at each point is attained based on the condition number metric. Take the logarithm of the condition number and then normalize the result.

$$J_a = \begin{bmatrix} 1 & 0 & 0 & 0 \\ 0 & 1 & -1 & 0 \\ 0 & 1 & 1 & 0 \\ 0 & 0 & 0 & 1 \end{bmatrix}. \tag{18}$$

The matrix $\begin{bmatrix} q_2 \\ q_3 \end{bmatrix} = \begin{bmatrix} 1 & -1 \\ 1 & 1 \end{bmatrix} \begin{bmatrix} a_2 \\ a_3 \end{bmatrix}$ in J_a describes the motion trend. When actuators 2 and 3 at the universal joint are pressurized, q_2 is not changed while q_3 increases. When actuator 2 pressurized and actuator 3 contracted, q_2 increases while q_3 is not changed. This assumption also simplifies the kinematic mapping between actuation and configuration space, while the motion trend is not violated.

The compliance of a single finger is depicted in Fig. 10(a)–10(c), where the logarithm of the metric is taken and normalized. K_b represents the stiffness in the object coordinate system. Fig. 10(a) shows the compliance cloud obtained using σ_1, and Fig. 10(c) shows the compliance cloud derived from σ_2. Similar to manipulability, the compliance ellipsoid has a larger volume (σ_2) in areas where the ellipsoid is more singular (yellow regions), as shown in Fig. 10(b). In addition, it can be observed from the heatmaps of both diagrams that the variation of σ_1 is greater than that of σ_2.

V. Experimental Validation

The objective of this section is to validate the performance of both the hardware and the proprioception system of the DexCo hand system. This validation process is composed of three distinct parts: verification at the actuator level, at the proprioception system level, and at the overall robotic hand level. Hand-level validations, including grasping strength, grasping cycle time, finger strength, and finger repeatability, are referred to the benchmark [85], where these four validations are proposed. In addition, following this benchmark, we propose the twisting strength validation to test the adduction/abduction capability of the hand. In conclusion, this section primarily introduces these experimental setups and separately discusses the results of each experiment. The key to the DexCo hand's ability to accomplish various tasks lies in its excellent performance specs, its dexterity

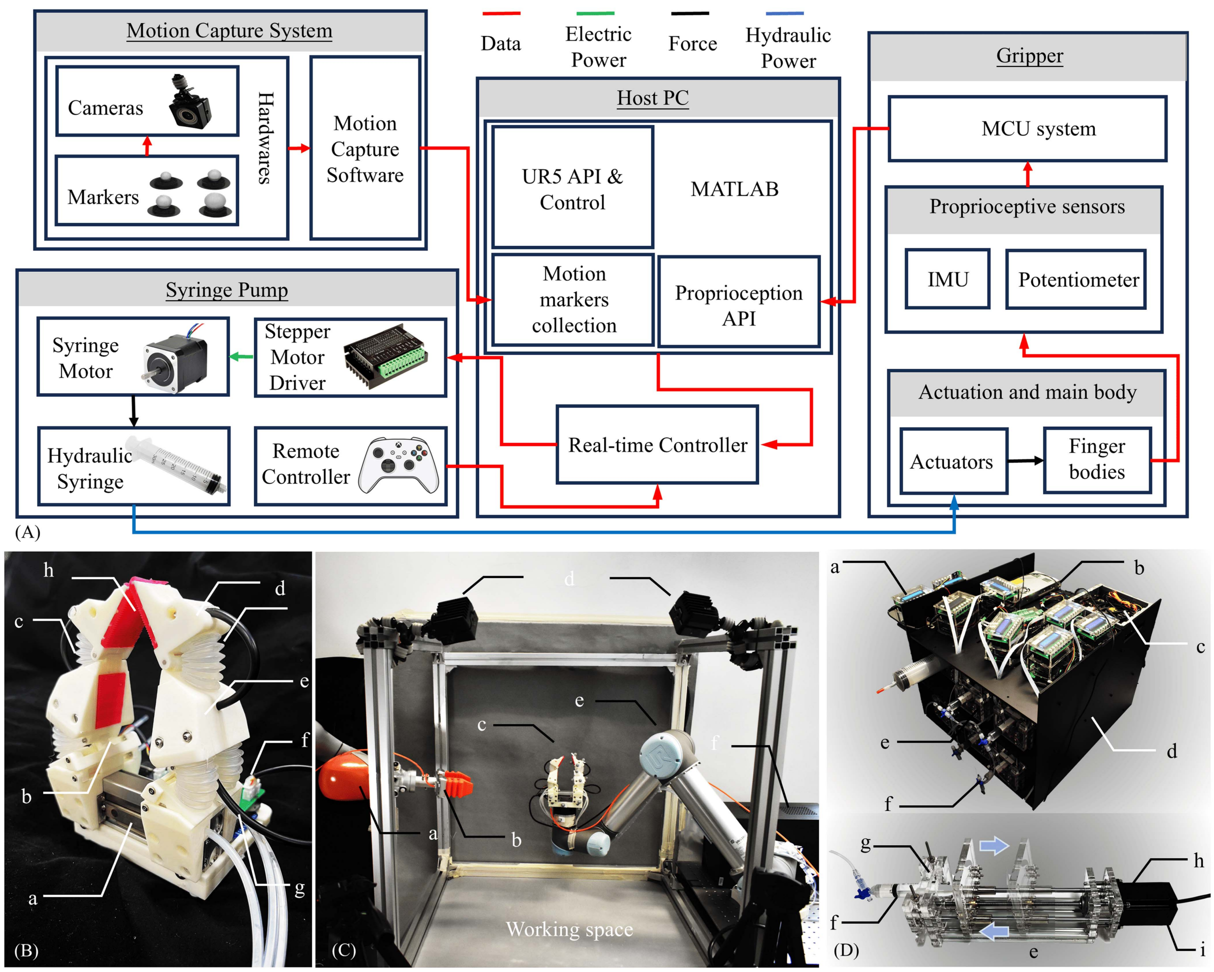

Fig. 11. System setup. (A) System blocks. (B) DexCo hand: (a) pneumatic palm; (b) universal joint; (c) hydraulic actuator; (d) 3-D printed fingertip; (e) 3D printed proximal link; (f) PCB circuit and Arduino MCU; (g) IMU cable; and (h) soft pad. (C) Experimental setup: (a) KUKA iiwa arm; (b) a normal soft gripper; (c) the DexCo hand; (d) cameras of the motion capture system (Optitracker); (e) UR 5 arm; and (f) Host PC. (D) Syringe pump system: (a) stepper motor driver; (b) 24-V dc power; (c) stepper motor controller; (d) acrylic syringe pump box; (e) syringe pump; (f) hydraulic syringe; (g) syringe locker; (h) stepper motor; and (i) electromagnetic encoder.

in mimicking a human hand, and the compliance that simplifies control, as evidenced by the experimental results.

A. *Experimental System Setup*

We adopted benchmarks proposed by Falco et al. [85] to assess the robotic hand's performance, categorizing functional indicators into grasping strength, finger strength, and grasping cycle time. In addition, to account for the hand's capability in nonplanar operations, we introduced a functional indicator for torsional force inspired by the benchmark. However, the assessment of dexterity and compliance lacks a universally accepted benchmark, treated as an open question in this article. Rather than conducting quantitative experiments for dexterity and compliance, we demonstrate these qualities practically through the hand's task completion, showcasing its compliance and dexterity in an observable manner.

The experimental setup encompasses three platforms: the actuator platform, the proprioception system platform, and the robotic hand test platform. The experimental platform is illustrated in Fig. 11(A) and 11(C). The platform consists of five components: a motion capture system, a syringe pump system, a UR5 system, the robotic hand system, and a host computer [see Fig. 11(A)]. Reflective markers on each link of the robotic hand, captured by motion cameras in the Optitrack system, enable the calculation of the hand's configuration space. The syringe pump system, with eight independent pumps, controls actuator expansion and contraction directly, with data collection and transmission to the host computer. The robotic hand, equipped with origami actuators, IMUs, linear potentiometers, Arduino, and peripheral circuits, communicates configuration space information to the host computer. Data collection and high-level control commands, such as UR5 movement positions and finger speed, are facilitated through MATLAB interfaces.

The actuator testing platform comprises a single-channel syringe pump [see Fig. 11(D)], an origami actuator, a linear guide, and a force sensor. DexCo hand-related tests involve the UR5, DexCo hand [see Fig. 11(B)], two single-axis force sensors [see Fig. 13(b)], a six-axis sensor, and a data acquisition card.

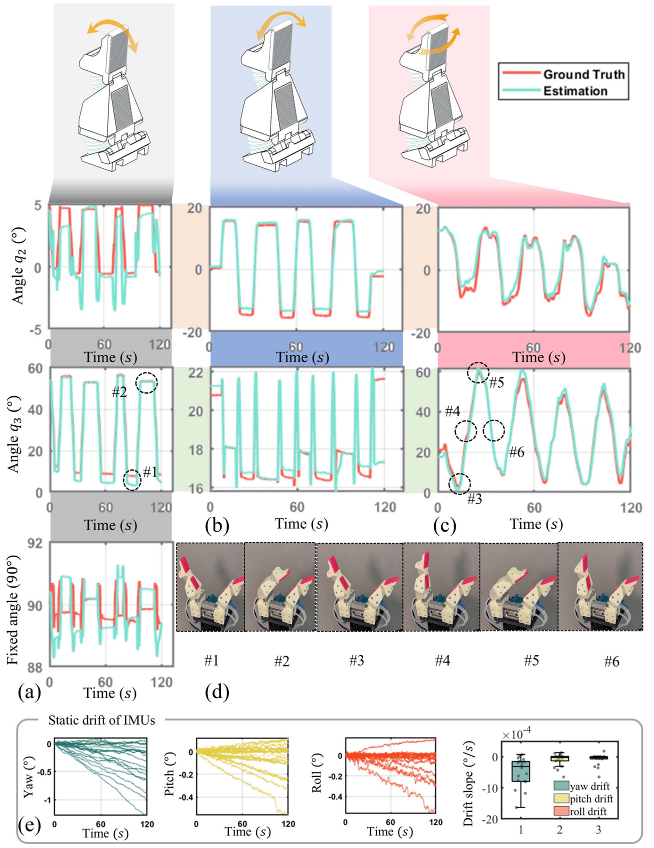

Fig. 12. Position feedback of IMU in all motions. (a) Position feedback in flexion of the proximal link. The constant angle, 90°, has small variants (about 2°) in the solution. (b) Position in adduction/abduction of the proximal link. The jumping change happens due to the collision between the proximal link and base link. (c) Position feedback in normal motion. (d) Hand Motions. Poses #1 and #2 fit with the time of q_3 figure in (a). Poses #3–#6 fit with the time of q_3 figure in (c). (e) IMU drift in static and the drift slope distribution.

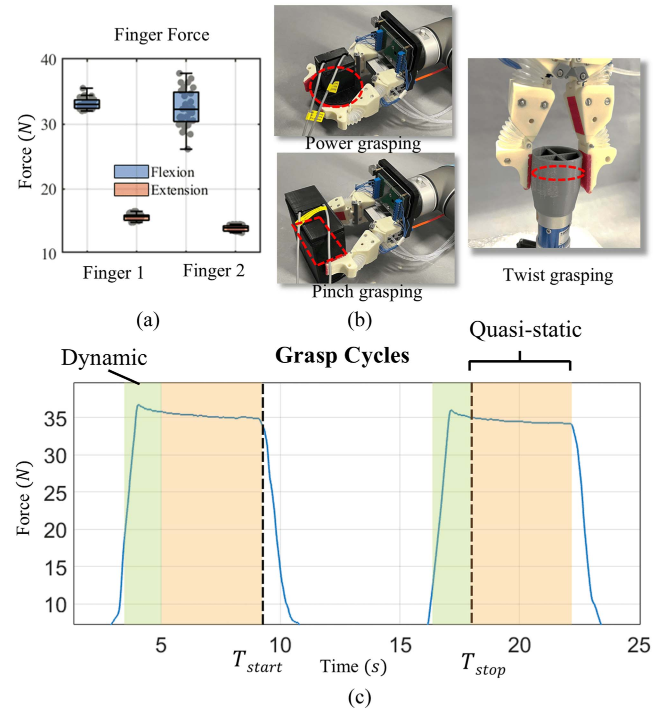

Fig. 13. (a) Finger strength experiment. Finger 1 is finger in good condition. Finger 2 is finger with air in a hydraulic actuator. (b) Experimental setup in tests, including grasping strength, grasp cycle time, repeatability, and twisting strength. A rectangular box is grasped in pinch test. A cylindrical box is grasped in power grasping test. (c) Force–time pattern in grasping strength and grasp cycle time experiments.

Algorithm 1: Steps for Grasp Strength Validation.

Require: $A_s, G_{\text{type}}, q_{\text{init}}, \rho_0$ ▷ artifact size, grasp type, initial joint position of the hand, number of cycles
$q \leftarrow \text{config}(G_{\text{type}}, A_s)$ ▷ desired joint angles
$\rho \leftarrow 0$ ▷ current grasp cycle
while $\rho_0 - \rho > 0$ **do**
  hand.goto (q_{init}) ▷ fully open the hand
  hand.goto (q) ▷ fully close the hand
  wait (t_s) ▷ stabilize force data
  $f \leftarrow$ sensor.observemean() hfill/>▷ collect force
  $\rho \leftarrow \rho + 1$ ▷ update grasp cycle
end while

B. Hydraulic Actuator Local Compliance Validation

In this experiment, the origami actuators are locked in the same way as in the robotic hand, with one end fixed to a uniaxial force sensor and the other end to a linear slide. The hydraulic actuators are connected to the syringe pump, simulating the state of the actuators under actuation. During the experiment, the syringe pump drives the origami actuator from its shortest length to its maximum length (23–33.5 mm), with each interval being 1.5 mm [as shown in Fig. 6(h)]. At each driven length, the linear slide stretches and compresses the actuator within a range that does not cause severe yielding, with a total displacement of about 30 mm and an incremental displacement of 1 mm each time. This reciprocating test was repeated three times, and the average force at each position was used as the measure of force exerted at that position.

As shown in Fig. 6(h), the range of force exerted by the actuator lies between −122.4 and 27.4 N. The longer the actuator (higher h_0), the weaker its ability to be stretched positively; conversely, the shorter the actuator, the weaker its ability to be compressed. The bottom of Fig. 6(h) shows the difference between theoretical and actual forces, denoted as $|\Delta F|$. This difference is greatest near $h_0 = 23$ mm, primarily because, at this length, the actuator has the most prominent unexpected deformation on the origami shell.

C. Proprioception Validation

In this experiment, we conducted tests focusing on both stability and accuracy. In the accuracy experiment, we gathered sensor data and motion capture system data, while the DexCo hand assumed different postures. The motion capture system provided spatial pose data for the finger link, serving as the ground truth for the robotic hand's posture. The configuration space of the robotic hand was calculated based on (5). We collected ground truth and IMU data five times for each posture, averaging the values. The average values were then converted to the robotic hand's configuration space for comparison, allowing us to assess

Algorithm 2: Steps for Finger Strength Validation.

Require: F_{type} , M_{type} , q_{init} , ρ_0 ▷ finger type, motion type, initial joint position of the hand, number of cycles
1: $q \leftarrow \text{config}(F_{\text{type}}, M_{\text{type}})$ ▷ desired joint angles
2: $\rho \leftarrow 0$ ▷ current cycle
3: **while** $\rho_0 - \rho > 0$ **do**
4: hand.goto (q_{init}) ▷ fully open the hand
5: hand.goto (q) ▷ fully close the hand
6: wait (t_s) ▷ stabilize force data
7: $f \leftarrow$ sensor.observemean () ▷ collect force
8: $\rho \leftarrow \rho + 1$ ▷ update grasp cycle
9: **end while**

the accuracy of the IMU in estimating the dexterous hand's posture. Further details on the calibration method between the IMU and ground truth can be found in Appendix A.

The DexCo hand performed three representative actions: flexion, adduction/abduction, and mixed. Results displayed in Fig. 12(a)–12(c) indicate that the IMU's accuracy is commendable, with a deviation in configuration space ranging approximately from $0°$ to $5°$, depending on the situation. Notably, in Fig. 12(a), where the expected result is $90°$, some fluctuations are observed. This is attributed to the use of an optimization-based calibration method, introducing slight deviations.

The stability experiment focuses on the IMU data drift. Employing the same setup as the accuracy experiment, the DexCo hand maintained stillness in various posture, while 2-min data are collected for each posture [see Fig. 12(e)]. The distribution of the drift slope is shown in Fig. 12(e), where the average drift slope is $[-0.49, -0.10, -0.09] \times 10^{-3}$ for yaw pitch and roll. The residual sum of squares, $\sum(y - y_{\text{fit}})^2$, which can be used to describe the data drift stability, is [0.64°, 0.08°, 0.20°] for yaw pitch and roll. Overall, based on our experience, utilizing the system for up to 10 min during manipulation poses no issues.

D. Grasping Strength Validation

Grasp strength serves as a crucial indicator of a robotic hand's capability to apply maximum force to an object. For the experiment, 3-D-printed artifacts were split into two parts to facilitate both pinch and wrap grasps. Pinch grasp tests utilized five block-shaped artifacts, while wrap grasp tests involved four cylindrical artifacts. Force sensors were secured with rubber bands at both ends to prevent shear forces. As shown in Algorithm 2, given the artifact size and grasp type, position control was applied to the hand to reach the desired configuration, where the number of cycles ρ is 32 in the experiment.

To ensure accuracy, the sum of force readings from each tandem pressure sensor was taken. A quasi-static grasp force was employed to determine the true strength of the end-effector, disregarding the first and last 10% of nonzero data in each cycle. The remaining middle 80% was used to calculate the average combined force (F_{total}). Mean, standard deviation, and 95% confidence interval were calculated based on the average of all 32 cycles.

Table IV presents the grasp strength results for different grasp types and artifact size dimensions. Power grasping strength remained relatively consistent across artifact sizes, whereas pinch grasp strength increased with larger artifact sizes. Notably, power grasping exhibited higher strength than pinch grasping (20.14–22.4 N) for the same size, ranging from 24.83 to 27.16 N, attributed to a significant portion of the grasping strength being directed in the shear direction during power grasp tests. In addition, a downward trend in grasp strength during cycling indicates that potential durability testing may be required for this end-effector.

E. Grasping Cycle Time Validation

Grasp cycle time is the time taken by a robotic hand to close and open from a pregrasp configuration to a grab position and back. The experiment setup and procedure for conducting the grasp cycle time test is the same as the grasp force test (see Algorithm 2). The grasp cycle begins when the end-effector begins to close from a fully open initial attitude and ends when the finger is opened after the grasp has been performed. T_{cycle} is defined by two adjacent cycles, T_{start} and T_{stop} , as shown in Fig. 13(c), where T_{start} marks the time when the quasi-static force is removed from the artifact at the end of each grasp, and T_{stop} occurs at the point in time when the dynamic force has stabilized to a quasi-static.

The grasp cycle time for every individual grasp was computed using the equation $T_{\text{cycle}} = T_{\text{stop}} - T_{\text{start}}$. The grasp cycle time data for nine artifacts were compared for both grasp types of our end-effector, as shown in Table V. Irrespective of the type of grasp, there exists a correlation between artifact size and the grasp cycle time, wherein the cycle time tends to decrease as artifact size increases. However, it is noteworthy that the pinch test (1.02–2.04 s) exhibits a more pronounced decreasing trend in cycle time as compared to the wrap test (1.33–1.40 s).

F. Finger Strength Validation

Our methodology for measuring finger force is similar to the previous experimental setup. Each finger pushes against a pinch box [see Fig. 13(b)], while the pinch box is securely anchored to the ground in this test. The procedure entailed a series of standardized steps executed for each finger (see Algorithm 1). Given the finger type and motion type, position control was applied to the hand to reach the desired configuration. Similar to the grasp strength validation, the DexCo hand was instructed to repeatedly fully open and close, and mean force is collected in a quasi-static period, with ρ set as 32 and t_s set as 5 s.

Finger 1 is newly manufactured; Finger 2 is heavily used for two days. The most prominent difference between fingers 1 and 2 is the air bubbles in the hydraulic actuator. In the hydraulic actuator of finger 2, one-sixth of the volume is empty in a fully extended state. Therefore, the comparison of fingers 1 and 2 shows the effect of air bubbles on hydraulic actuators and indicates the difference between hydraulic actuation and pneumatic actuation. Table VI and Fig. 13(a) show the strength performance of two fingers. First, the air bubbles have little effect on the maximum average finger force. However, in the

TABLE VI
FINGER STRENGTH DATA FOR TWO FINGERS WITH DIFFERENT MOTION TYPES

Finger	Motion types	Avg finger strength (N)	Stdev (N)	95% confidence interval (N)
1	Flexion	34.83	0.80	$[34.54, 36.12]$
	Extension	15.64	0.46	$[15.48, 15.81]$
2	Flexion	34.43	2.75	$[33.44, 35.43]$
	Extension	13.88	0.41	$[13.73, 14.03]$

TABLE VII
FINGER REPEATABILITY

Finger	Avg offset distance (mm)	Stdev (mm)	95% confidence interval (mm)
1	−0.03	0.08	$[-0.06, 0.00]$
2	−0.69	0.43	$[-0.85, -0.54]$

Algorithm 3: Steps for Finger Repeatability Validation.

Require: F_{type} , q_{init} , ρ_0 $\triangleright$ finger type, initial joint position of the hand, number of cycles
$q_a, q_b, q_c \leftarrow$ config (F_{type}) $\triangleright$ three different desired joint angles
$\rho \leftarrow 0$ $\triangleright$ current cycle
while $\rho_0 - \rho > 0$ **do**
  hand.goto $(q_{\text{init}}$
  $d_0 \leftarrow$ sensor.observe () $\triangleright$ initial displacement
  hand.goto (q_a)
  hand.goto (q_b)
  hand. goto(q_c)
hand. goto (q_{init}) $\triangleright$ back to initial configuration
  $d \leftarrow$ sensor.observe() $\triangleright$ final displacement
  $\rho \leftarrow \rho + 1$ $\triangleright$ update grasp cycle
  offset $\leftarrow abs(d - d_0)$ $\triangleright$ offset in current cycle
end while

experiment, finger 2 requires a larger displacement to reach the maximum finger force (34.43 N for flexion and 13.88 N for extension). Second, the air bubbles greatly enlarge the standard deviation. This could be because of the reduced finger precision when there are bubbles in hydraulic actuators.

G. Finger Repeatability Validation

Finger repeatability measures how consistently a finger can reach the same position from the same direction. The accuracy of finger repeatability is tested using a linear displacement sensor that provides unidirectional measurement accuracy of 0.02 mm. The test requires the finger to move to four unique positions before returning to the starting position, covering most of the finger's workspace. As shown in Algorithm 3, q_a, q_b, q_c, and q_{init} are completely disengaged by actuating each joint. The number of cycles ρ is 32 in the experiment.

Finger 1, with a 0.03-mm repeatability accuracy, demonstrates performance closely aligned with that of a conventional rigid hand (see Table VII), thereby exhibiting better repeatability compared to Finger 2 (0.69-mm repeatability accuracy).

Algorithm 4: Steps for Twist Strength Validation.

Require: $A_s, q_{\text{init}}, \rho_0$ $\triangleright$ artifact size, initial joint position of the hand, number of cycles
$q \leftarrow \text{config}(A_s)$ $\triangleright$ desired joint angles for fully close
$\boldsymbol{\theta} \leftarrow \text{trajectory}(A_s)$ $\triangleright$ joint trajectory for twist
$\rho \leftarrow 0$
while $\rho_0 - \rho > 0$ **do**
  hand.goto (q_{init}) $\triangleright$ fully open the hand
  hand.goto (q) $\triangleright$ fully close the hand
  hand.excute $(\boldsymbol{\theta})$ $\triangleright$ perform twist motion
  wait (t_s) $\triangleright$ stabilize toruqe data
  $\tau \leftarrow$ sensor.observemean () $\triangleright$ collect torque
  $\rho \leftarrow \rho + 1$ $\triangleright$ update grasp cycle
end while

TABLE VIII
TWIST STRENGTH FOR DIFFERENT SIZED OBJECTS

Artifact size (mm)	Avg torque (N·m)	Stdev (N·m)	95% confidence interval (N·m)
30	0.082	0.016	$[0.076, 0.088]$
50	0.229	0.038	$[0.215, 0.242]$
70	0.428	0.058	$[0.407, 0.449]$
90	0.587	0.050	$[0.579, 0.615]$

H. DexCo Hand Twisting Strength Validation

Based on the existing benchmarks [85], we introduce the twist strength benchmark to evaluate robotic hands. The twist strength of a robotic hand refers to the highest amount of torque generated by the pinch grasp [see Fig. 13(b)]. The torque sensor's rotational axis was oriented perpendicular to the palm during a pinch grasp. As shown in Algorithm 4, the DexCo hand is first instructed to its fully open configuration. Then, fingers are commanded to the fully close state, such that the hand achieves a maximum grasp force before twisting. Finally, the DexCo hand implements the twisting motion $\boldsymbol{\theta}$ at this maximum pinch force to measure the maximum torque under quasi-static conditions, where $\boldsymbol{\theta}$ is any angle that ensures the hand twists to achieve the maximum torque. t_s is set as 5 s and ρ is 32 in this experiment.

We designed four artifacts to be mounted on the torque sensor. For each set of torque readings obtained from the torque sensor, the stabilized torque under quasi-static conditions was calculated for each cycle, as presented in Table VIII.

VI. DexCo Hand Fine In-Hand Manipulation

The DexCo hand has successfully achieved advanced manipulation capabilities across a range of fine in-hand tasks. Beyond typical pinch and power grasps, it excels in challenging scenarios such as cluttered picking, assembling light bulbs, and unscrewing bottle caps, even in constrained environments. In addition, it has succeeded in tasks previously unattainable by other dexterous hands, including opening plastic bags, counting cards, and sorting medications, highlighting its versatility in fine manipulation. Fig. 14 showcases these diverse tasks, consistent with the previously referenced material:

1) *The light bulb assembly task* [see Fig. 14(a)] involves tightening and then unscrewing the bulb using the

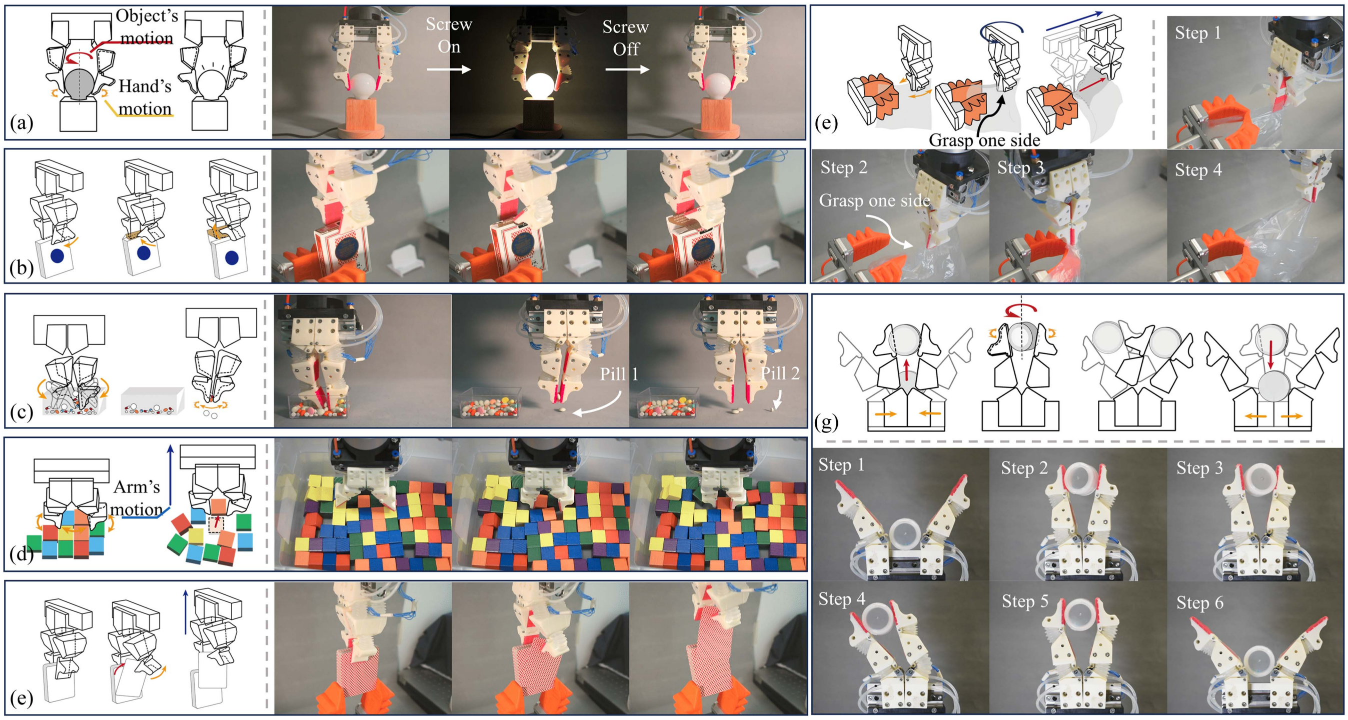

Fig. 14. Fine in-hand manipulation demonstration. (a) Screw on and screw off a real light bulb. (b) Card box opening. (c) Picking and sorting pills based on size with in-finger manipulation. (d) Cluttered bin picking with finger–environmental interaction. (e) Counting cards and taking card out one by one. (f) Plastic bag opening. (g) Typical caging manipulation and in-hand rotation.

DexCo hand's forward and backward twisting motions. To demonstrate its compliance, the hand's central axis is offset from the bulb's axis on the xy plane. A wider palm requires greater joint flexion to grip the object, and as flexion increases, the y-axis motion range decreases. The palm's width adjusts the twisting range accordingly.

2) *Card box opening* task is shown in Fig. 14(b). The box's top end has a semicircular opening, typically opened by inserting fingers. The DexCo hand employs a similar mechanism, opening the box from above using its flexion DoFs or the side using its adduction/abduction DoFs. During this process, the robot arm remains stationary.
3) *Pill sorting* is depicted in Fig. 14(c). The process includes picking multiple pills from a pile and then categorizing them into different piles using fine in-hand manipulation. This task requires the DexCo hand to utilize its fingertip dexterity to pick a portion of the pills from a cluttered arrangement, followed by separating the small particles using fingertip sliding, akin to the human hand sprinkling powder.
4) *Cluttered bin picking* [see Fig. 14(d)] features dense hand–environment interaction, which is a great challenge for robots to operate in an unstructured environment. In the real word, pick and place is not enough because objects are always stacked or gathered in a confined space. From our result, the dexterity at the fingertip of the DexCo hand demonstrates a great capability to manipulate in clutter. We believe that the manipulation for grasping capability of the DexCo hand can solve this cluttered bin picking challenge.
5) *Card-counting* task is illustrated in Fig. 14(e). Human hands use the thumb and index finger to swiftly extract cards from a deck, with the other hand assisting. The DexCo hand mimics this, with the orange soft hand holding the deck for assistance. The DexCo hand uses its fingertip dexterity to first separate the top card, with no arm movement. Once the card is separated, the arm moves upwards to extract it. Without this fine in-hand manipulation, consecutive cards would be removed together.
6) *Opening a plastic bag* is shown in Fig. 14(f). The soft orange hand, attached to the end of a KUKA robot, adjusts its opening and closing through pneumatic control. This task involves initially manipulating the unopened, transparent, thin plastic bag with the fingertips to open it and grip one edge. The bag is then repositioned for the soft hand to grasp the other edge, and the DexCo hand pulls it open. The success of the bag-opening phase depends on the dexterity and compliance of the fine in-hand manipulation. During the bag-stretching phase, sufficient gripping force is required while pinching with the DexCo hand.
7) *Caging manipulation and in-hand rotation* [see Fig. 14(g)] depicts two sliding primitives along the x and y axes and two translation primitives along the y and z axes, as classified by Dollar et al. [1]. The palm's role here is to extend the range of sliding, perform translational movement, and accommodate a wider range of object diameters. The hand's local compliance also increases the safety margin during manipulation, reducing control difficulty.

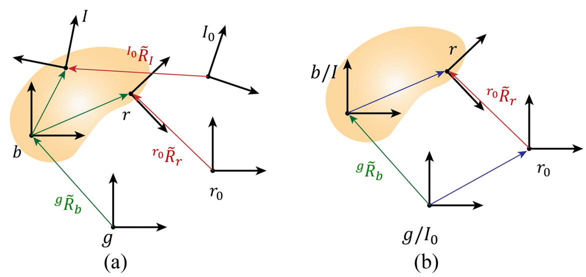

Fig. 15 (a) Frames of the rigid body. (b) Substituted frames of the rigid body.

VII. Conclusion and Future Work

This study has introduced the DexCo hand system, which successfully mimics human fine in-hand manipulation capabilities. By leveraging soft hydraulic actuation, the DexCo hand achieves a balance between control complexity, dexterity, compliance, and motion accuracy. Experimental results have demonstrated its ability to perform complex tasks such as screwing light bulbs, opening plastic bags, and counting cards, showcasing its versatility in real-world applications. The integration of soft actuation and proprioceptive feedback allows for more nuanced and precise manipulation, addressing challenges that have long hindered the field of robotics. The DexCo hand's compact and compliant design holds great promise for advancing the capabilities of robotic systems in a range of environments, from industrial settings to everyday tasks.

Future research will focus on enhancing the DexCo hand's ability to autonomously perform a broader range of tasks, particularly in unstructured environments. Improving the integration of sensory feedback for real-time adjustments and more delicate object handling will be a key objective. Additional efforts will be made to optimize the hand's design for greater durability and energy efficiency in repetitive or continuous operations. Investigating machine learning algorithms to enable the DexCo hand to self-adapt to varying task demands will further extend its capabilities, allowing for more intelligent manipulation strategies. Finally, expanding its applications in sectors such as health care, manufacturing, and service industries will be explored to fully leverage the system's potential.

Appendix A
IMU Calibration Method

A complete rigid body calibration system is shown in Fig. 15(a), which includes the current pose of IMU denoted as $\{I\}$, the current pose of ground truth sensor denoted as $\{r\}$, the body-fixed frame $\{b\}$, the initial frame of IMU denoted as $\{I_0\}$, the initial frame of ground truth sensor denoted as $\{r_0\}$, and the world frame denoted as $\{g\}$. The frames $\{I\}$, $\{r\}$, and $\{b\}$ are attached to the rigid body, while the frames $\{I_0\}$, $\{r_0\}$, and $\{g\}$ are attached to the ground. The representation of $\{I\}$ and $\{r\}$ in $\{g\}$ is shown as follows:

$$\begin{cases} {}^{g}\tilde{R}_b \cdot {}^{b}R_I = {}^{g}\tilde{R}_I \\ {}^{g}\tilde{R}_b \cdot {}^{b}R_r = {}^{g}\tilde{R}_r. \end{cases} \tag{19}$$

The calibration objective is to find the transformation relationship between ${}^{g}\tilde{R}_I$ and ${}^{g}\tilde{R}_r$. Without loss of generality, we make the following two substitutions.

1) *Assumption 1:* let $\{g\} = \{I_0\}$, i.e., ${}^{g}R_{I_0} = I$.
2) *Assumption 2:* let $\{b\} = \{I\}$, i.e., ${}^{g}R_I = I$.

We can simplify the coordinate system, as shown in Fig. 15(b). Moreover, we can obtain

$${}^{g}\tilde{R}_b {}^{b}R_r = {}^{g}R_{r_0} {}^{r_0}\tilde{R}_r. \tag{20}$$

Our goal is to collect IMU and ground truth data from two different positions, ${}^{g}_{1}\tilde{R}_b, {}^{r}_{1}\tilde{R}_{r_0}$ and ${}^{g}_{2}\tilde{R}_b, {}^{r}_{2}\tilde{R}_{r_0}$, respectively, to obtain two parameter matrices ${}^{b}R_r$ and ${}^{g}R_{r_0}$. We have

$${}^{g}_{1}\tilde{R}_b \cdot {}^{b}R_r \cdot {}^{r}_{1}\tilde{R}_{r_0} = {}^{g}_{2}\tilde{R}_b \cdot {}^{b}R_r \cdot {}^{r}_{2}\tilde{R}_{r_0}. \tag{21}$$

To obtain ${}^{b}R_r$, we formulate the aforementioned equation as a nonlinear optimization problem

$$\begin{aligned} \text{Minimize} \quad & f(R) = \left\| R \cdot {}^{r}_{1}\tilde{R}_{r_0} \cdot {}^{r}_{2}\tilde{R}_{r_0} - {}^{g}_{1}\tilde{R}_b \cdot {}^{g}_{2}\tilde{R}_b \cdot R \right\|_F \\ \text{subject to} \quad & R^T \cdot R = I \\ & \det(R) = 1. \end{aligned}$$

In this context, $\|\cdot\|_F$ denotes the Frobenius norm. By employing this optimization approach, it is possible to find ${}^{b}R_r$ and ${}^{g}R_{r_0}$ that closely approximate the ground truth values.

Appendix B
Ellipse in Matrix

Considering a matrix A as follows:

$$\begin{bmatrix} x \\ y \end{bmatrix}^T \begin{bmatrix} 5 & 4 \\ 4 & 5 \end{bmatrix} \begin{bmatrix} x \\ y \end{bmatrix} = x^T A x = 1 \tag{22}$$

where A is a positive-definite matrix. The eigenvalues are $\lambda_1 = 1$ and $\lambda_2 = 9$, and the normalized eigenvectors are $\mu_1 = \begin{bmatrix} \frac{1}{\sqrt{2}} \\ -\frac{1}{\sqrt{2}} \end{bmatrix}$ and $\mu_2 = \begin{bmatrix} \frac{1}{\sqrt{2}} \\ \frac{1}{\sqrt{2}} \end{bmatrix}$. We can then decompose A orthogonally

$$A = Q\Lambda Q^{-1} = Q\Lambda Q^T = \begin{bmatrix} \frac{1}{\sqrt{2}} & \frac{1}{\sqrt{2}} \\ -\frac{1}{\sqrt{2}} & \frac{1}{\sqrt{2}} \end{bmatrix} \begin{bmatrix} 1 & 0 \\ 0 & 9 \end{bmatrix} \begin{bmatrix} \frac{1}{\sqrt{2}} & -\frac{1}{\sqrt{2}} \\ \frac{1}{\sqrt{2}} & \frac{1}{\sqrt{2}} \end{bmatrix} \tag{23}$$

where

$$\begin{aligned} P(f) &= x^T A x = x^T Q \Lambda Q^T x \\ &= \left(Q^T x\right)^T \Lambda \left(Q^T x\right) \\ &= 1\left(\frac{x-y}{\sqrt{2}}\right)^2 + 9\left(\frac{x+y}{\sqrt{2}}\right)^2. \end{aligned} \tag{24}$$

The relationship between the axes of an ellipse and the eigenvectors of the matrix A can be observed. The length of the semiaxis can be calculated as the square of the inverse of the eigenvalue of A.

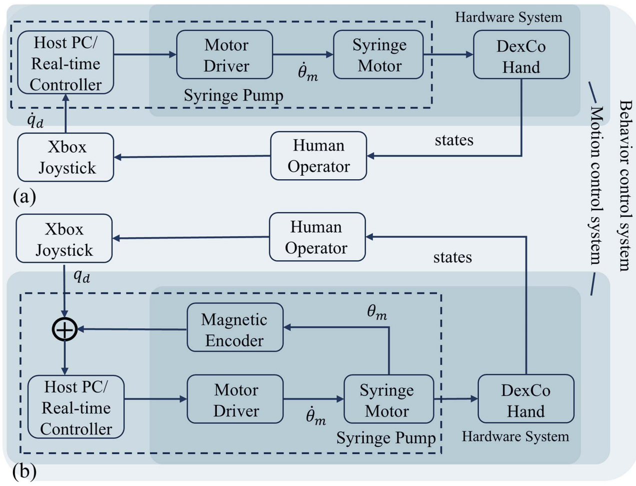

Fig. 16 Hierarchical control blocks. (a) Teleoperated joint velocity control of the DexCo hand. (b) Teleoperated joint position control of the DexCo hand.

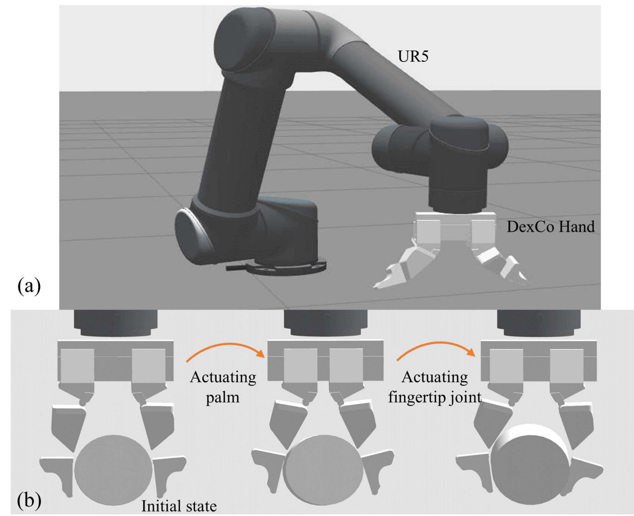

Fig. 17. Simulator for DexCo hand. (a) Integration with UR5. (b) Illustration of active motion and passive compliance in simulator.

APPENDIX C
TELEOPERATED CONTROL FOR VARIOUS TASKS

The DexCo hand is teleoperated to accomplish the manipulation tasks, rather than hard coding. An Xbox joystick can intuitively control seven DoFs of the DexCo hand, including six DoFs for the motion of two fingers and one DoFs for the palm motion and stiffness. In this article, we implemented two controllers controlling the position [see Fig. 16(b)] and velocity [see Fig. 16(a)] of the hand.

For the velocity control, as shown in Fig. 16(a), the joystick sends out the desired velocity commands, $\dot{q}_d$, to the real-time controller, which is a proportional–integral–derivative (PID) controller with an inverse kinematic computation based on (18). The syringe motor is controlled in an open-loop under velocity control mode. Pressed button represents a fixed velocity, while the stick and trigger map to a continuous velocity range.

For the position control, as shown in Fig. 16(b), the joystick sends the desired position commands, q_d, to the real-time controller, where a PID controller takes in the error and sends the control output $\dot{\theta}_m$. By using a magnetic encoder for feedback, we can control the stepper motor at a high frequency. In the position control mode, the stick space, $[-1, 1] \in \Re^2$, and trigger space, $[0, 1] \in \Re$, are mapped to a specific position of the joint.

APPENDIX D
SIMULATOR FOR DEXCO HAND WITH SOFT HYDRAULIC ACTUATION MECHANISM

We implement the DexCo hand as a ROS package for simulation, which could also be treated as a case study for compliance modeling. Based on (18), we substitute the parameters in Jacobian with the kinematics structure

$$\begin{bmatrix} q_1 \\ q_2 \\ q_3 \\ q_4 \end{bmatrix} = \begin{bmatrix} 1 & 0 & 0 & 0 \\ 0 & 37 & -37 & 0 \\ 0 & 33.3 & 33.3 & 0 \\ 0 & 0 & 0 & 66.7 \end{bmatrix} \begin{bmatrix} h_1 \\ h_2 \\ h_3 \\ h_4 \end{bmatrix} = \boldsymbol{J}_a \boldsymbol{h} \tag{25}$$

where $\boldsymbol{h}$ represents the actuation space for one finger. Based on the Jacobian, we can easily transform the motion, force, and linear stiffness between the configuration space $\boldsymbol{q}$ and actuation space $\boldsymbol{h}$, as shown in Tables II and III. The variable stiffness property inherent in the DexCo hand can be modeled as linear elastic force or nonlinear elastic force as shown in the following equations:

$$\boldsymbol{\tau}_k = -\boldsymbol{k}\left(\boldsymbol{q}_0\right) \Delta \boldsymbol{q} \tag{26}$$

$$\boldsymbol{\tau}_k = \boldsymbol{f}\left(\boldsymbol{q}_0, \Delta \boldsymbol{q}\right) \tag{27}$$

where $\boldsymbol{q}_0$ is the joint angle without external force, $\boldsymbol{q}$ is the current joint angle, and $\Delta \boldsymbol{q} = \boldsymbol{q} - \boldsymbol{q}_0$ represents the current deformation. The linear elastic force, (26), can be transformed based on the stiffness matrix, $K_a = J_a^T K_q J_a$. The nonlinear elastic force, (27), which is more accurate in describing the motion of the DexCo hand, cannot be directly transformed using the stiffness matrix.

By modeling the stiffness as force in simulation, it should affect the dynamics in simulation as the following way:

$$\boldsymbol{M}\ddot{\boldsymbol{q}} + \boldsymbol{H}(\dot{\boldsymbol{q}}, \boldsymbol{q}) = \boldsymbol{\tau}_k \tag{28}$$

where the left-hand side represents the terms of inertial force, Coriolis force, and gravity, which are developed by the simulator, while the right-hand side represents the torques at the joints. $\boldsymbol{\tau}_k$ is the torque generated from deformation. Implementing the torque $\boldsymbol{\tau}_k$, we can successfully simulate the behavior of the nonlinear variable stiffness elastic force.

Fig. 17(a) shows the simulator in gazebo. The UR5 can be automatically controlled by MOVEit, while the DexCo hand is controlled by joint position signals. It is worth noting that the simulator of DexCo hand fully simulates the hydraulic position control in actuation space by treating it as variable stiffness relation [see (26) or (27)]. Fig. 17(b) presents the nonlinear variable stiffness property in grasping and manipulating a cylinder. The palm is first commanded to close without actuating other joints, where those joints adapt to the object. Then, the fingertip is actuated for further manipulation.

Acknowledgment

Pieter Abbeel holds concurrent appointments as a Professor at UC Berkeley and as an Amazon Scholar. This paper describes work performed at UC Berkeley and is not associated with Amazon.

References

[1] A. M. Dollar, "Classifying human hand use and the activities of daily living," in *The Hum. Hand an Inspiration Robot Hand Develop.*. Cham, Switzerland: Springer, 2014, pp. 201–216.

[2] A. Billard and D. Kragic, "Trends and challenges in robot manipulation," *Science*, vol. 364, no. 6446, 2019, Art. no. eaat8414.

[3] A. Bicchi, "Hands for dexterous manipulation and robust grasping: A difficult road toward simplicity," *IEEE Trans. Robot. Autom.*, vol. 16, no. 6, pp. 652–662, Dec. 2000.

[4] M. R. Cutkosky, "On grasp choice, grasp models, and the design of hands for manufacturing tasks," *IEEE Trans. Robot. Autom.*, vol. 5, no. 3, pp. 269–279, Jun. 1989.

[5] S. Puhlmann, J. Harris, and O. Brock, "RBO Hand 3: A platform for soft dexterous manipulation," *IEEE Trans. Robot.*, vol. 38, no. 6, pp. 3434–3449, Dec. 2022.

[6] A. S. Morgan, K. Hang, B. Wen, K. Bekris, and A. M. Dollar, "Complex in-hand manipulation via compliance-enabled finger gaiting and multi-modal planning," *IEEE Robot. Autom. Lett.*, vol. 7, no. 2, pp. 4821–4828, Apr. 2022.

[7] A. Bhatt, A. Sieler, S. Puhlmann, and O. Brock, "Surprisingly robust in-hand manipulation: An empirical study," 2022, *arXiv:2201.11503*.

[8] J. Zhou et al., "A soft-robotic approach to anthropomorphic robotic hand dexterity," *IEEE Access*, vol. 7, pp. 101483–101495, 2019.

[9] T. Chen, M. Tippur, S. Wu, V. Kumar, E. Adelson, and P. Agrawal, "Visual dexterity: In-hand reorientation of novel and complex object shapes," *Sci. Robot.*, vol. 8, no. 84, 2023, Art. no. eadc9244.

[10] J. Pitz, L. Röstel, L. Sievers, and B. Bäuml, "Dextrous tactile in-hand manipulation using a modular reinforcement learning architecture," in *Proc. IEEE Int. Conf. Robot. Autom.*, 2023, pp. 1852–1858.

[11] I. Guzey, B. Evans, S. Chintala, and L. Pinto, "Dexterity from touch: Self-supervised pre-training of tactile representations with robotic play," 2023, *arXiv:2303.12076*.

[12] A. Rodriguez and M. T. Mason, "Grasp invariance," *Int. J. Robot. Res.*, vol. 31, no. 2, pp. 236–248, 2012.

[13] A. Rodriguez and M. T. Mason, "Effector form design for 1DOF planar actuation," in *Proc. IEEE Int. Conf. Robot. Autom.*, 2013, pp. 349–356.

[14] R. F. Shepherd et al., "Multigait soft robot," *Proc. Nat. Acad. Sci.*, vol. 108, no. 51, pp. 20400–20403, 2011.

[15] Y. Cui, X. An, Z. Lin, Z. Guo, X.-J. Liu, and H. Zhao, "Design and implementation of an underactuated gripper with enhanced shape adaptability and lateral stiffness through semi-active multi-degree-of-freedom endoskeletons," *Int. J. Robot. Res.*, vol. 43, no. 6, pp. 873–896, 2024.

[16] J. Zhou et al., "Adaptive variable stiffness particle phalange for robust and durable robotic grasping," *Soft Robot.*, vol. 7, no. 6, pp. 743–757, 2020.

[17] L. Li et al., "Stiffness-tunable soft gripper with soft-rigid hybrid actuation for versatile manipulations," *Soft Robot.*, vol. 9, no. 6, pp. 1108–1119, 2022.

[18] W. Wan, K. Harada, and F. Kanehiro, "Planning grasps with suction cups and parallel grippers using superimposed segmentation of object meshes," *IEEE Trans. Robot.*, vol. 37, no. 1, pp. 166–184, Feb. 2021.

[19] W. Ruotolo, D. Brouwer, and M. R. Cutkosky, "From grasping to manipulation with gecko-inspired adhesives on a multifinger gripper," *Sci. Robot.*, vol. 6, no. 61, 2021, Art. no. eabi9773.

[20] Y. Zhai et al., "Desktop fabrication of monolithic soft robotic devices with embedded fluidic control circuits," *Sci. Robot.*, vol. 8, no. 79, 2023, Art. no. eadg3792.

[21] D. M. Vogt et al., "Shipboard design and fabrication of custom 3D-printed soft robotic manipulators for the investigation of delicate deep-sea organisms," *PLoS One*, vol. 13, no. 8, 2018, Art. no. e0200386.

[22] N. Fazeli, M. Oller, J. Wu, Z. Wu, J. B. Tenenbaum, and A. Rodriguez, "See, feel, act: Hierarchical learning for complex manipulation skills with multisensory fusion," *Sci. Robot.*, vol. 4, no. 26, 2019, Art. no. eaav3123.

[23] M. T. Mason and J. K. Salisbury Jr, "*Robot Hands and the Mechanics of Manipulation*. Cambridge, MA, USA: MIT Press, 1985.

[24] M. Bauza, F. R. Hogan, and A. Rodriguez, "A data-efficient approach to precise and controlled pushing," in *Proc. Conf. Robot Learn.*, 2018, pp. 336–345.

[25] A. Zeng, S. Song, J. Lee, A. Rodriguez, and T. Funkhouser, "TossingBot: Learning to throw arbitrary objects with residual physics," *IEEE Trans. Robot.*, vol. 36, no. 4, pp. 1307–1319, Aug. 2020.

[26] N. C. Dafle et al., "Extrinsic dexterity: In-hand manipulation with external forces," in *Proc. IEEE Int. Conf. Robot. Autom.*, 2014, pp. 1578–1585.

[27] A. Rodriguez, M. T. Mason, and S. Ferry, "From caging to grasping," *Int. J. Robot. Res.*, vol. 31, no. 7, pp. 886–900, 2012.

[28] R. Deimel and O. Brock, "A novel type of compliant and underactuated robotic hand for dexterous grasping," *Int. J. Robot. Res.*, vol. 35, nos. 1–3, pp. 161–185, 2016.

[29] Y.-H. Liu, "Computing n-finger form-closure grasps on polygonal objects," *Int. J. Robot. Res.*, vol. 19, no. 2, pp. 149–158, 2000.

[30] B. Siciliano, *Springer Handbook of Robotics*, vol. 2. Berlin, Germany: Springer-Verlag, 2008, pp. 15–35.

[31] M. T. Mason, S.S. Srinivasa, and A. S. Vazquez, "Generality and simple hands," in *Proc. 14th Int. Symp. Robot. Res.*, 2011, pp. 345–361.

[32] M. Ciocarlie et al., "The Velo gripper: A versatile single-actuator design for enveloping, parallel and fingertip grasps," *Int. J. Robot. Res.*, vol. 33, no. 5, pp. 753–767, 2014.

[33] D. Yoon and Y. Choi, "Analysis of fingertip force vector for pinch-lifting gripper with robust adaptation to environments," *IEEE Trans. Robot.*, vol. 37, no. 4, pp. 1127–1143, Aug. 2021.

[34] Y.-J. Kim, H. Song, and C.-Y. Maeng, "BLT gripper: An adaptive gripper with active transition capability between precise pinch and compliant grasp," *IEEE Robot. Autom. Lett.*, vol. 5, no. 4, pp. 5518–5525, Oct. 2020.

[35] S. Yuan, L. Shao, C. L. Yako, A. Gruebele, and J. K. Salisbury, "Design and control of Roller Grasper V2 for in-hand manipulation," in *Proc. IEEE/RSJ Int. Conf. Intell. Robots Syst.*, 2020, pp. 9151–9158.

[36] S. Yuan, A. D. Epps, J. B. Nowak, and J. K. Salisbury, "Design of a roller-based dexterous hand for object grasping and within-hand manipulation," in *Proc. IEEE Int. Conf. Robot. Autom.*, 2020, pp. 8870–8876.

[37] W. G. Bircher, A. S. Morgan, and A. M. Dollar, "Complex manipulation with a simple robotic hand through contact breaking and caging," *Sci. Robot.*, vol. 6, no. 54, 2021, Art. no. eabd2666.

[38] A. M. Dollar and R. D. Howe, "The highly adaptive SDM hand: Design and performance evaluation," *Int. J. Robot. Res.*, vol. 29, no. 5, pp. 585–597, 2010.

[39] L. U. Odhner et al., "A compliant, underactuated hand for robust manipulation," *Int. J. Robot. Res.*, vol. 33, no. 5, pp. 736–752, 2014.

[40] A. J. Spiers, A. S. Morgan, K. Srinivasan, B. Calli, and A. M. Dollar, "Using a variable-friction robot hand to determine proprioceptive features for object classification during within-hand-manipulation," *IEEE Trans. Haptics*, vol. 13, no. 3, pp. 600–610, Jul–Sep. 2020.

[41] R. R. Ma, L. U. Odhner, and A. M. Dollar, "A modular, open-source 3D printed underactuated hand," in *Proc. IEEE Int. Conf. Robot. Autom.*, 2013, pp. 2737–2743.

[42] L. U. Odhner and A. M. Dollar, "Stable, open-loop precision manipulation with underactuated hands," *Int. J. Robot. Res.*, vol. 34, no. 11, pp. 1347–1360, 2015.

[43] K. Hang, A. S. Morgan, and A. M. Dollar, "Pre-grasp sliding manipulation of thin objects using soft, compliant, or underactuated hands," *IEEE Robot. Autom. Lett.*, vol. 4, no. 2, pp. 662–669, Apr. 2019.

[44] R. R. Ma, A. Spiers, and A. M. Dollar, "M2 gripper: Extending the dexterity of a simple, underactuated gripper," in *Advances in Reconfigurable Mechanisms and Robots II*. Berlin, Germany: Springer, 2016, pp. 795–805.

[45] B. Calli and A. M. Dollar, "Vision-based model predictive control for within-hand precision manipulation with underactuated grippers," in *Proc. IEEE Int. Conf. Robot. Autom.*, 2017, pp. 2839–2845.

[46] W. G. Bircher, A. M. Dollar, and N. Rojas, "A two-fingered robot gripper with large object reorientation range," in *Proc. IEEE Int. Conf. Robot. Autom.*, 2017, pp. 3453–3460.

[47] L. U. Odhner, R. R. Ma, and A. M. Dollar, "Open-loop precision grasping with underactuated hands inspired by a human manipulation strategy," *IEEE Trans. Autom. Sci. Eng.*, vol. 10, no. 3, pp. 625–633, Jul. 2013.

[48] J. Zhou, X. Chen, J. Li, Y. Tian, and Z. Wang, "A soft robotic approach to robust and dexterous grasping," in *Proc. IEEE Int. Conf. Soft Robot.*, Apr. 2018, pp. 412–417.

[49] W. Zhu et al., "A soft-rigid hybrid gripper with lateral compliance and dexterous in-hand manipulation," *IEEE/ASME Trans. Mechatron.*, vol. 28, no. 1, pp. 104–115, Feb. 2023.

[50] J. Xia et al., "Discrete pneumatic-tendon-coupled actuators with interconnected air circuit for untethered soft robots," *Adv. Intell. Syst.*, Dec. 2024, Art. no. 2400533.
[51] J. K. Salisbury and B. Roth, "Kinematic and force analysis of articulated mechanical hands," in *J. Mech., Transmiss., Autom. Des.*, vol. 105, pp. 35–41, 1983.
[52] M. Quigley, C. Salisbury, A. Y. Ng, and J. K. Salisbury, "Mechatronic design of an integrated robotic hand," *Int. J. Robot. Res.*, vol. 33, no. 5, pp. 706–720, 2014.
[53] M. G. Catalano, G. Grioli, E. Farnioli, A. Serio, C. Piazza, and A. Bicchi, "Adaptive synergies for the design and control of the Pisa/IIT SoftHand," *Int. J. Robot. Res.*, vol. 33, no. 5, pp. 768–782, 2014.
[54] C. D. Santina, C. Piazza, G. Grioli, M. G. Catalano, and A. Bicchi, "Toward dexterous manipulation with augmented adaptive synergies: The Pisa/IIT SoftHand 2," *IEEE Trans. Robot.*, vol. 34, no. 5, pp. 1141–1156, Oct. 2018.
[55] J. M. Inouye and F. J. Valero-Cuevas, "Anthropomorphic tendon-driven robotic hands can exceed human grasping capabilities following optimization," *Int. J. Robot. Res.*, vol. 33, no. 5, pp. 694–705, 2014.
[56] "Allegro hand v4.0—Allegro hand," 2024. [Online]. Available: https://www.allegrohand.com/
[57] "Shadow dexterous hand series—Research and development tool," 2024. [Online]. Available: https://www.shadowrobot.com/dexterous-hand-series/
[58] J. Zhou, S. Chen, and Z. Wang, "A soft-robotic gripper with enhanced object adaptation and grasping reliability," *IEEE Robot. Autom. Lett.*, vol. 2, no. 4, pp. 2287–2293, Oct. 2017.
[59] C. B. Teeple, T. N. Koutros, M. A. Graule, and R. J. Wood, "Multi-segment soft robotic fingers enable robust precision grasping," *Int. J. Robot. Res.*, vol. 39, no. 14, pp. 1647–1667, 2020.
[60] O. Shorthose, A. Albini, L. He, and P. Maiolino, "Design of a 3D-printed soft robotic hand with integrated distributed tactile sensing," *IEEE Robot. Autom. Lett.*, vol. 7, no. 2, pp. 3945–3952, Apr. 2022.
[61] R. Ozawa, Y. Mishima, and Y. Hirano, "Design of a transmission with gear trains for underactuated mechanisms," *IEEE Trans. Robot.*, vol. 32, no. 6, pp. 1399–1407, Dec. 2016.
[62] D. M. Aukes et al., "Design and testing of a selectively compliant underactuated hand," *Int. J. Robot. Res.*, vol. 33, no. 5, pp. 721–735, 2014.
[63] R. Ozawa, H. Kobayashi, and K. Hashirii, "Analysis, classification, and design of tendon-driven mechanisms," *IEEE Trans. Robot.*, vol. 30, no. 2, pp. 396–410, Apr. 2014.
[64] A. Kargov, T. Werner, C. Pylatiuk, and S. Schulz, "Development of a miniaturised hydraulic actuation system for artificial hands," *Sens. Actuators A: Phys.*, vol. 141, no. 2, pp. 548–557, 2008.
[65] P. Polygerinos et al., "Soft robotics: Review of fluid-driven intrinsically soft devices; manufacturing, sensing, control, and applications in human-robot interaction," *Adv. Eng. Mater.*, vol. 19, no. 12, 2017, Art. no. 1700016.
[66] J. Huang et al., "Modular origami soft robot with the perception of interaction force and body configuration," *Adv. Intell. Syst.*, vol. 4, no. 9, 2022, Art. no. 2200081.
[67] T. G. Thuruthel, B. Shih, C. Laschi, and M. T. Tolley, "Soft robot perception using embedded soft sensors and recurrent neural networks," *Sci. Robot.*, vol. 4, no. 26, 2019, Art. no. eaav1488.
[68] J. Zhou, Y. Chen, X. Chen, Z. Wang, Y. Li, and Y. Liu, "A proprioceptive bellows (PB) actuator with position feedback and force estimation," *IEEE Robot. Autom. Lett.*, vol. 5, no. 2, pp. 1867–1874, Jan. 2020.
[69] L. Birglen, T. Laliberté, and C. M. Gosselin, *Underactuated Robotic Hands*, vol. 40. Berlin, Germany: Springer, 2007.
[70] D. Rus and M. T. Tolley, "Design, fabrication and control of soft robots," *Nature*, vol. 521, no. 7553, pp. 467–475, 2015.
[71] K. Hang, W. G. Bircher, A. S. Morgan, and A. M. Dollar, "Manipulation for self-identification, and self-identification for better manipulation," *Sci. Robot.*, vol. 6, no. 54, 2021, Art. no. eabe1321.
[72] K. Hang, W. G. Bircher, A. S. Morgan, and A. M. Dollar, "Hand–object configuration estimation using particle filters for dexterous in-hand manipulation," *Int. J. Robot. Res.*, vol. 39, no. 14, pp. 1760–1774, 2020.
[73] A. S. Morgan, W. G. Bircher, and A. M. Dollar, "Towards generalized manipulation learning through grasp mechanics-based features and self-supervision," *IEEE Trans. Robot.*, vol. 37, no. 5, pp. 1553–1569, Oct. 2021.
[74] J. Shi, J. Z. Woodruff, P. B. Umbanhowar, and K. M. Lynch, "Dynamic in-hand sliding manipulation," *IEEE Trans. Robot.*, vol. 33, no. 4, pp. 778–795, Aug. 2017.
[75] H. Wang et al., "Folding and bending planar coils for highly precise soft angle sensing," *Adv. Mater. Technol.*, vol. 5, no. 11, 2020, Art. no. 2000659.
[76] V. Sundaram et al., "Embedded magnetic sensing for feedback control of soft HASEL actuators," *IEEE Trans. Robot.*, vol. 39, no. 1, pp. 808–822, Feb. 2023.
[77] L. Biagiotti, F. Lotti, C. Melchiorri, and G. Vassura, "How far is the human hand? A review on anthropomorphic robotic end-effectors," University of Bologna, Tech. Rep., 2004.
[78] I. Kapandji, "The physiology of the joints, Volume I, upper limb," *Amer. J. Phys. Med. Rehabil.*, vol. 50, no. 2, 1971, Art. no. 96.
[79] L. Wang and Z. Wang, "Mechanoreception for soft robots via intuitive body cues," *Soft Robot.*, vol. 7, no. 2, pp. 198–217, 2020.
[80] J. Zhou, J. Huang, X. Ma, A. Lee, K. Kosuge, and Y.-H. Liu, "Design, modeling, and control of soft syringes enabling two pumping modes for pneumatic robot applications," *IEEE/ASME Trans. Mechatron.*, vol. 29, no. 2, pp. 889–901, Apr. 2024.
[81] N. Vahrenkamp, T. Asfour, G. Metta, G. Sandini, and R. Dillmann, "Manipulability analysis," in *Proc. 12th IEEE-RAS Int. Conf. Humanoid Robots*, 2012, pp. 568–573.
[82] K. L. Doty, C. Melchiorri, E. M. Schwartz, and C. Bonivento, "Robot manipulability," *IEEE Trans. Robot. Autom.*, vol. 11, no. 3, pp. 462–468, Jun. 1995.
[83] H. Jiang et al., "Hierarchical control of soft manipulators towards unstructured interactions," *Int. J. Robot. Res.*, vol. 40, no. 1, pp. 411–434, 2021.
[84] M. R. Cutkosky and I. Kao, "Computing and controlling compliance of a robotic hand," *IEEE Trans. Robot. Autom.*, vol. 5, no. 2, pp. 151–165, Apr. 1989.
[85] J. Falco et al., "Benchmarking protocols for evaluating grasp strength, grasp cycle time, finger strength, and finger repeatability of robot end-effectors," *IEEE Robot. Autom. Lett.*, vol. 5, no. 2, pp. 644–651, Apr. 2020.

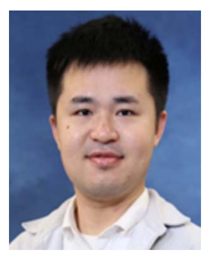

Jianshu Zhou (Member, IEEE) received the Ph.D. degree in mechanical engineering from the University of Hong Kong, Hong Kong, in 2020.

He was a Visiting Scholar and an incoming Postdoctoral Researcher with the Mechanical Systems Control Lab, Department of Mechanical Engineering, University of California at Berkeley, Berkeley, CA, USA. Prior to this, he was a Research Assistant Professor with the Chinese University of Hong Kong, Hong Kong. His research interests include robotics, grasping and manipulation, soft robotics, and robotic hands.

Junda Huang received the B.Eng. degree in automation from the University of Science and Technology of China, Hefei, China, in 2020. He is currently working toward the Ph.D. degree with the Chinese University of Hong Kong, Hong Kong.

His research interests include robotics, robotic grasping and manipulation, and robot control.

Qi Dou (Member, IEEE) received the B.Eng. degree in biomedical engineering from Beihang University, Beijing, China, in 2014, and the Ph.D. degree in computer science from the Chinese University of Hong Kong (CUHK), Hong Kong, in 2018.

From 2018 to 2020, she was a Postdoctoral Researcher with the Department of Computing, Imperial College London, London, U.K. She is currently an Assistant Professor with the Department of Computer Science and Engineering, CUHK. Her research interests include interdisciplinary field of artificial intelligence for medical scenarios, with expertise in medical image analysis, and robotic surgery perception.

Pieter Abbeel (Fellow, IEEE) received the B.S. and M.S. degrees in electrical engineering from Katholieke Universiteit Leuven, Leuven, Belgium, in 2000, and the Ph.D. degree in computer science from Stanford University, Standford, CA, USA, in 2008.

In fall 2008, he joined the Faculty of the University of California at Berkeley, Berkeley, CA, USA, with an appointment with the Department of Electrical Engineering and Computer Sciences. He holds concurrent appointments as a Professor with the University of California at Berkeley and as an Amazon Scholar. His current research interests include robotics and machine learning with a particular focus on challenges in personal robotics, surgical robotics, and connectomics.

Dr. Abbeel has won numerous awards, including Best Paper Awards at International Conference on Machine Learning and IEEE International Conference on Robotics and Automation, the Sloan Fellowship, the Air Force Office of Scientific Research Young Investigator Program Award, the Office of Naval Research Young Investigator Program Award, the Darpa Young Faculty Award, the Okawa Foundation Award, the TR35, the IEEE Robotics and Automation Society Early Career Award, and the Dick Volz Best U.S. Ph.D. Thesis in Robotics and Automation Award.

Yunhui Liu (Fellow, IEEE) received the Ph.D. degree in applied mathematics and information physics from the University of Tokyo, Tokyo, Japan, in 1992.

After working as a Research Scientist with the Electrotechnical Laboratory of Japan, he joined the Chinese University of Hong Kong (CUHK), Hong Kong, in 1995. He is currently the Choh-Ming Li Professor of Mechanical and Automation Engineering and the Director of the T Stone Robotics Institute, CUHK. He is the Director/CEO of the Hong Kong Centre for Logistics Robotics, sponsored by the InnoHK program of the Hong Kong government. He is an Adjunct Professor with the State Key Laboratory of Robotics Technology and System, Harbin Institute of Technology, Harbin, China. With more than 500 papers published in refereed journals and conference proceedings, he was listed as a Highly Cited Author (Engineering) by Thomson Reuters in 2013. His research interests include visual servoing, logistics robotics, medical robotics, multifingered grasping, mobile robots, and machine intelligence.

Dr. Liu has received numerous research awards from prestigious international journals, conferences in robotics and automation, and government agencies. He was the Editor-in-Chief for *Robotics and Biomimetics*, an Associate Editor for IEEE TRANSACTIONS ON ROBOTICS AND AUTOMATION, and the General Chair of the 2006 IEEE/RSJ International Conference on Intelligent Robots and Systems.